ORNL/TM-13157

OAK RIDGE NATIONAL LABORATORY

MARTIN MARIETTA

NONLINEAR ANALYSIS OF MACHINING DATA

L. M. Hively
N. E. Clapp
C. S. Daw
Oak Ridge National Laboratory

January 1996

CAUTION

This document has not been given final patent clearance and is for internal use only. If this document is to be given public release, it must be cleared through the site Technical Information Office which will see that the proper patent and technical information reviews are completed in accordance with Energy Systems Policy.

MANAGED BY
MARTIN MARIETTA ENERGY SYSTEMS, INC.
FOR THE UNITED STATES
DEPARTMENT OF ENERGY

DISCLAIMER

This report was prepared as an account of work sponsored by an agency of the United States Government. Neither the United States Government nor any agency thereof, nor any of their employees, make any warranty, express or implied, or assumes any legal liability or responsibility for the accuracy, completeness, or usefulness of any information, apparatus, product, or process disclosed, or represents that its use would not infringe privately owned rights. Reference herein to any specific commercial product, process, or service by trade name, trademark, manufacturer, or otherwise, does not necessarily constitute or imply its endorsement, recommendation, or favoring by the United States Government or any agency thereof. The views and opinions of authors expressed herein do not necessarily state or reflect those of the United States Government or any agency thereof.

ORNL/TM-13157

NONLINEAR ANALYSIS OF MACHINING DATA

L. M. Hively
N. E. Clapp
C. S. Daw
Oak Ridge National Laboratory

January 1996

Prepared for
U.S. Department of Energy
Office of Defense Programs
under
CRADA #Y1295-0357

Prepared by the
Engineering Technology Division
Oak Ridge National Laboratory
Oak Ridge, TN 37831-8066
managed by
LOCKHEED MARTIN ENERGY RESEARCH CORPORATION
for the
U.S. DEPARTMENT OF ENERGY
under contract DE-AC05-96OR22464

The submitted manuscript has been authored by a contractor of the U.S. Government under contract No. DE-AC05-96OR22464. Accordingly, the U.S. Government retains a nonexclusive, royalty-free license to publish or reproduce the published form of this contribution, or allow others to do so, for U.S. Government purposes.

CONTENTS

LIST OF FIGURES vii

LIST OF TABLES ix

ABSTRACT xi

1. INTRODUCTION 1

2. DATA ACQUISITION AND LINEAR ANALYSIS 2

3. NONLINEAR ANALYSIS 18

4. RESULTS AND DISCUSSION 20

5. CONCLUSIONS 42

ACKNOWLEDGMENTS 43

REFERENCES 45

DISTRIBUTION 47

LIST OF FIGURES

Fig. 2.1 Coordinate system (x, y, z) for the tool-part configuration 3
Fig. 2.2 Typical time-serial plots of the y-component of force (non-chatter) 4
Fig. 2.3 Typical time-serial plots of the z-component of acceleration (non-chatter) 5
Fig. 2.4 Typical time-serial plots of the first motor current component (non-chatter) 6
Fig. 2.5 Fourier power spectra for the nine non-chatter data channels 7
Fig. 2.6 Typical time-serial plots of the y-component of force (chatter) 8
Fig. 2.7 Typical time-serial plots of the z-component of acceleration (chatter) 9
Fig. 2.8 Typical time-serial plots of the first motor current component (chatter) 10
Fig. 2.9 Typical time-serial plots of the x-component of acceleration 12
Fig. 2.10 Typical time-serial plots of the y-component of acceleration 13
Fig. 2.11 Typical time-serial plots of the z-component of acceleration 14
Fig. 2.12 Fourier power spectra of the x-component of acceleration 15
Fig. 2.13 Fourier power spectra of the y-component of acceleration 16
Fig. 2.14 Fourier power spectra of the z-component of acceleration 17
Fig. 4.1 MIF plots of dataset #091801 22
Fig. 4.2 Typical results for dataset #091801: D- and K-spectra, correlation integrals 23
Fig. 4.3 Attractor plots in (A_x, A_y, A_z) space 24
Fig. 4.4 Attractor plots from principal components analysis 26
Fig. 4.5 Positive-going Poincaré sections for $A_x = 0$ 27
Fig. 4.6 Negative-going Poincaré sections for $A_x = 0$ 28
Fig. 4.7 Positive-going Poincaré sections for $A_z = 0$ 29
Fig. 4.8 Negative-going Poincaré sections for $A_z = 0$ 30
Fig. 4.9 Positive-going Poincaré sections for $A_y = 0$ 31
Fig. 4.10 Negative-going Poincaré sections for $A_y = 0$ 33
Fig. 4.11 Positive-going return maps (lag = 1) for $A_x = 0$ 34
Fig. 4.12 Negative-going return maps (lag = 1) for $A_x = 0$ 35
Fig. 4.13 Positive-going return maps (lag = 2) for $A_z = 0$ 36
Fig. 4.14 Negative-going return maps (lag = 2) for $A_z = 0$ 37
Fig. 4.15 Negative-going return maps (lag = 1) for $A_y = 0$ 38
Fig. 4.16 Positive-going return maps (lag = 1) for $A_y = 0$ 39
Fig. 4.17 Normalized frequency distribution of return times for $A_y = 0$ 41

LIST OF TABLES

Table 4.1 Summary of analysis results 20

Table 4.2 Sequences of motion in Fig. 4.15c 40

ABSTRACT

We analyzed cutting dynamics of stainless steel in the non-chatter and chatter regimes, toward the ultimate objective of chatter control. We used linear methods (principal components analysis, Fourier power spectra) and nonlinear techniques (mutual information function, correlation dimension and entropy spectra, Poincaré sections, return maps). We sampled three accelerations (A) at various spindle speeds: x in the cutting direction (A_x), y along the depth of cut (A_y), and z in the feed direction (A_z). The correlation dimension is typically <4 on the embedded attractor above the noise floor. Non-chatter dynamics exist at low spindle speed, with low periodicity, low acceleration amplitude, and strong chaotic features. Chatter occurs at high spindle speed, with high acceleration amplitude, weak chaotic features, and strong period-1 motion. Period-1 and -2 dynamics dominate in the x and z directions, respectively. Poincaré sections for $A_y = 0$ are sensitive to the non-chatter-to-chatter transition, which involves a change from chaotic behavior to period-1 motion along the tool axis. Return maps and Poincaré sections show the non-chatter-to-chatter transition before detection by an experienced operator, and may serve as predicators of this transition. Our work also suggests some likely alternatives for chatter control.

1. INTRODUCTION

Advanced machining requires faster material removal rates, which usually results in poorer part quality, due to nonlinear tool-part dynamics. For example, tool chatter during lathe cutting results in nicks, gouges, and roughened surface finish. Such features are unacceptable for precision components. This work characterizes the nonlinear dynamics during lathe cutting in non-chatter and chatter regimes. The ultimate objective is control of chatter dynamics for faster material removal with the same (or better) part quality, which we plan to address in later work.

The theory of nonlinear dynamics provides a basis for understanding many complex physical and engineering systems. In this work, we apply nonlinear/chaos analysis to the experimental data for stainless steel machining on a lathe. Some technical literature exists on this problem [1-10]. Berger et al. [1] analyzed experimental tool-part accelerations in the pre- and mild-chatter regimes, and found the information dimensions of 2.38 and 2.51, respectively. Grabec [2-4] modeled cutting by two differential equations for the dynamics in the cutting direction (x) and depth of cut (y), and found chaotic features.

Jemielniak and Widota [5] modeled the cutting by a single differential equation for the depth of cut (y) with random disturbances due to the unpredictable nature of chip removal, and applied conventional stability analysis to the resulting chatter dynamics. Lin and Weng [6] also modeled the cutting with one differential equation and studied the linear and nonlinear stability properties of the dynamics. They found that linear theory predicts a stabilizing effect for an increase in feed rate and in the cutting tool stiffness. Their nonlinear stability analysis showed that chatter amplitude increases with an increase in cutting width or a decrease in feed rate.

Qu et al. [7] apply several nonlinear analysis tools to vibration data from rotating machinery (turbo-generator and compressor), demonstrating the usefulness of these tools in diagnosing nonlinear dynamics. Wu and Liu [8] developed a two-dimensional model for the cutting direction (x) and the depth of cut (y), including fluctuations in the mean friction coefficient due to chip removal. Wu and Liu [9] found that their model [8] is consistent with the experimental chatter dynamics, involving velocity dependency, vibration mode coupling, and chip generation. Bukkapatnam et al. [10] recently analyzed data from lathe cutting and found evidence for low dimensional choas. We found no publications with detailed nonlinear/chaos analysis of cutting data, or attempts to stop chatter via chaos control methods.

A practical issue for this analysis is robustness to noise and finite data precision, because previous work has found that noisy data are exceedingly difficult to analyze. This concern is an important one, since many nonlinear analysis tools handle only model data, which has no noise, is very precise (to 8 - 16 digits), and involves much data (10^5 - 10^6 points). Thus, we use tools that can cope with the noise (10 - 50% of the signal amplitude) and finite data precision (7 - 12 bits) in modest-length datasets (10^4 - 10^5 points), typical of experimental data.

This paper is organized as follows. Section 2 explains the data acquisition and linear analysis. Section 3 describes the features of specific nonlinear tools and their application to machining data. Section 4 provides a discussion of our results. Section 5 presents the conclusions of our work.

2. DATA ACQUISITION AND LINEAR ANALYSIS

We obtained our data during machining of a 316 stainless steel cylinder on a lathe (Monarch Mark Century 2000) in Building 9737 at the Y-12 Plant in Oak Ridge, Tennessee. The analog-to-digital converter recorded the data (in arbitrary units) with 12-bit precision (i.e., values between -2048 and +2047). Each dataset began with one line of header information, describing the machining conditions and sampling rate. The remainder of the dataset had time serial records (one line per record), with the following data at equal time intervals:

three orthogonal forces (F) in (x, y, z): F_x, F_y, F_z.

three orthogonal accelerations (A) in (x, y, z): A_x, A_y, A_z.

three currents (I_1, I_2, I_3.) from the three-phase power input to the lathe spindle motor.

The accelerometer calibration showed ±2% accuracy at ≤7 kilohertz, which rose to ±5% accuracy for ≤10 kilohertz. Accelerometer calibration above 10 kilohertz was unavailable. No calibration information was available for the current and force sensors. Figure 2.1 shows the (x, y, z) coordinate system for the tool-part configuration.

We obtained two datasets for an initial evaluation (the data acquisition setup, the choice of sampling frequency, sensor response with frequency, and data variability). The machining conditions for the non-chatter dataset were at a spindle speed of 62 revolutions per minute (RPM), 0.012-inch feed rate per revolution, and 0.01-inch depth of cut. The machining conditions for the chatter dataset were 133 RPM, 0.005-inch feed rate per revolution, and 0.02-inch depth of cut. Each dataset spanned 2 seconds at a sampling rate of 15 kilohertz, corresponding to 30,000 samples for each of the nine data channels.

Figures 2.2-2.4 show typical time-serial plots of force, acceleration, and motor current for the non-chatter regime. Figure 2.4 displays very clear steps in current amplitude, corresponding to very limited precision in this signal. The motor current value varied from 263 to 294 (a range of 31 units), corresponding to slightly less than 5 bits of precision in variability. The other two motor current channels had a variation over 20 and 32 units, respectively. This limited precision arose from the data acquisition setup, which could not be improved under our work scope. Figure 2.5 shows the Fourier power spectra for each of the nine data channels. The motor current spectra have poor resolution, due to the limited data precision. The force spectra had a noise floor above 2 kilohertz, indicating that the force sensors had a high frequency cutoff that could not be changed under our work scope. Acceleration spectra show much structure over the full frequency range (0 - 5 kilohertz), without a noise floor.

Figures 2.6-2.8 show typical time serial plots of force, acceleration, and motor current for the chatter regime. The precision limitation again appears in the motor current (Fig. 2.8). A frequency cutoff above 2000 Hertz also occurs in the force data (not shown). Even with these data limitations, clear correlations exist between the force and current data. We concluded the following from these observations: (a) further analysis of motor currents was inappropriate, due to limited data precision; (b) further analysis of forces was inappropriate, due to the frequency cutoff by the sensor; (c) analysis of accelerations requires a higher sampling rate to see the full dynamics, since no noise floor appears for a sampling rate of 15 kilohertz.

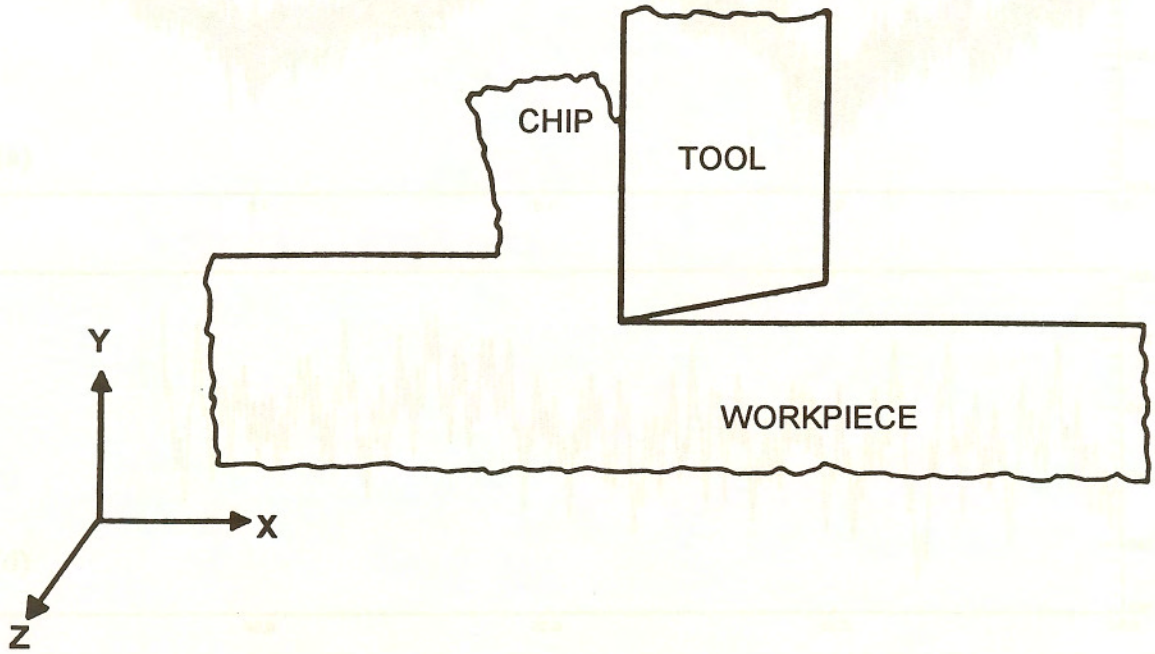

Fig. 2.1. Coordinate system (x, y, z) for the tool-part configuration.

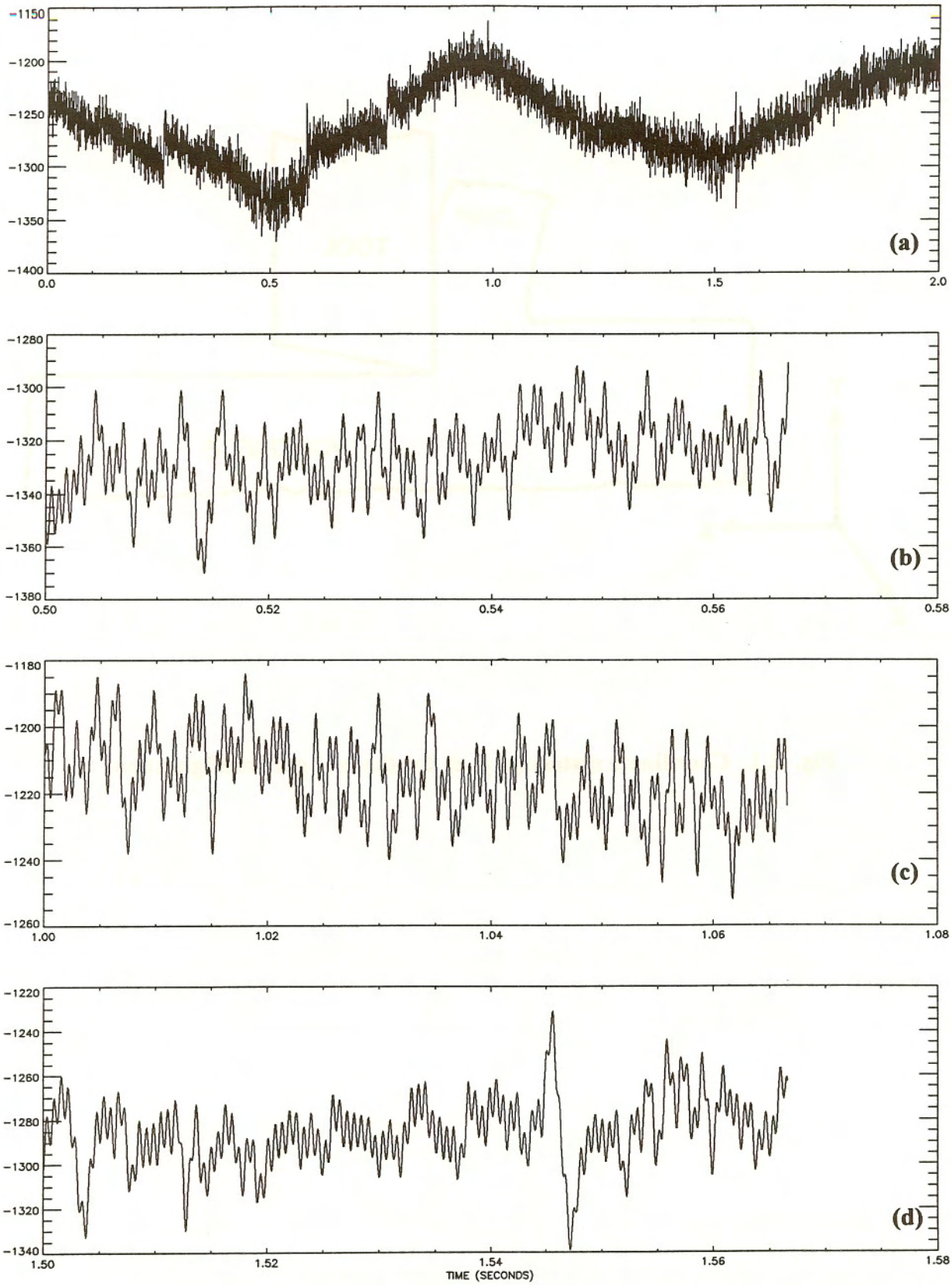

Fig. 2.2. Typical time-serial plots of the y-component of force in the non-chatter regime from (a) 0 - 2s, and expanded plots starting at (b) 0.5s, (c) 1.0s, and (d) 1.5 s.

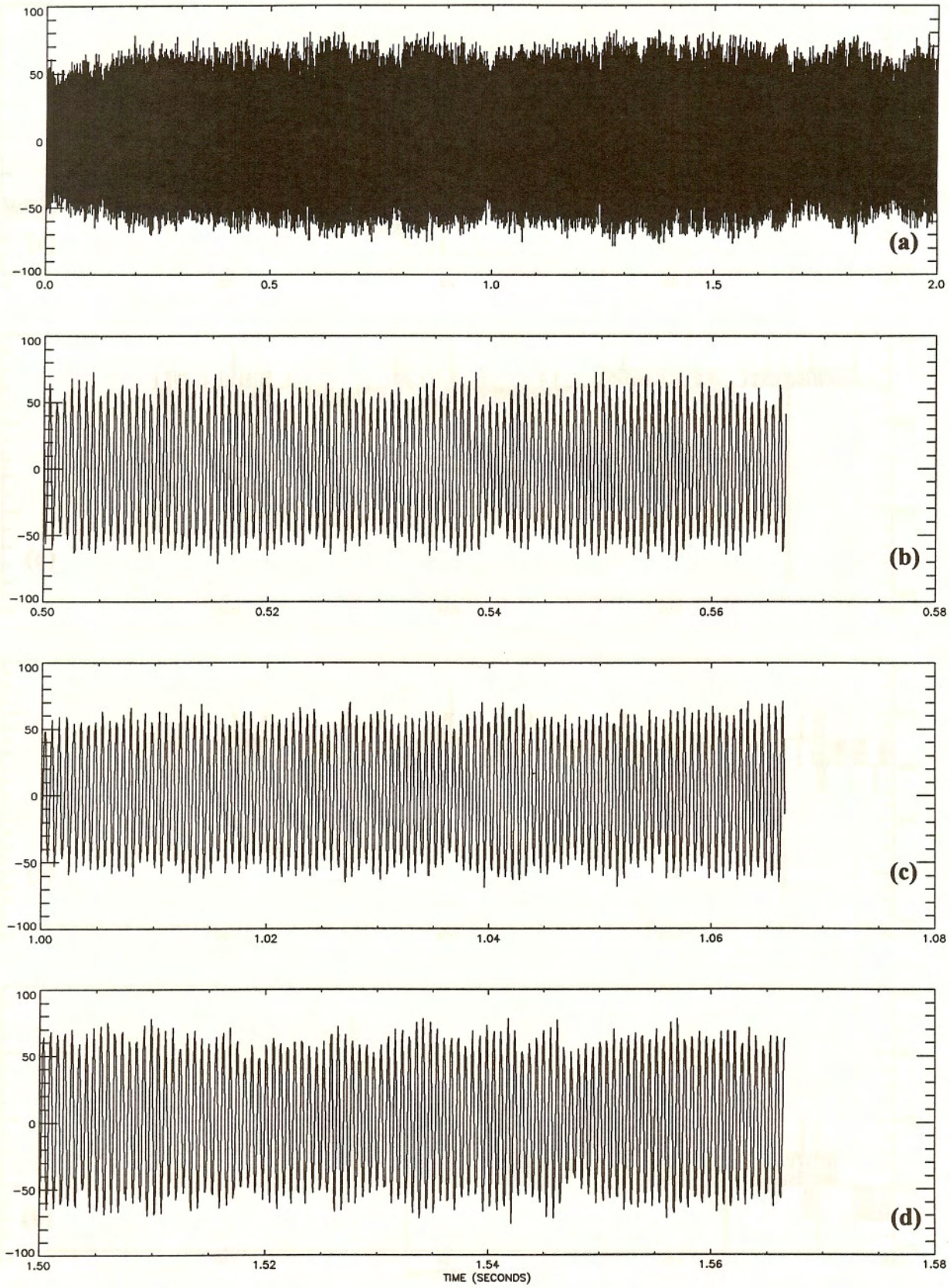

Fig. 2.3. Typical time-serial plots of the z-component of acceleration in the non-chatter regime from (a) 0 - 2s, and expanded plots starting at (b) 0.5s, (c) 1.0s, and (d) 1.5 s.

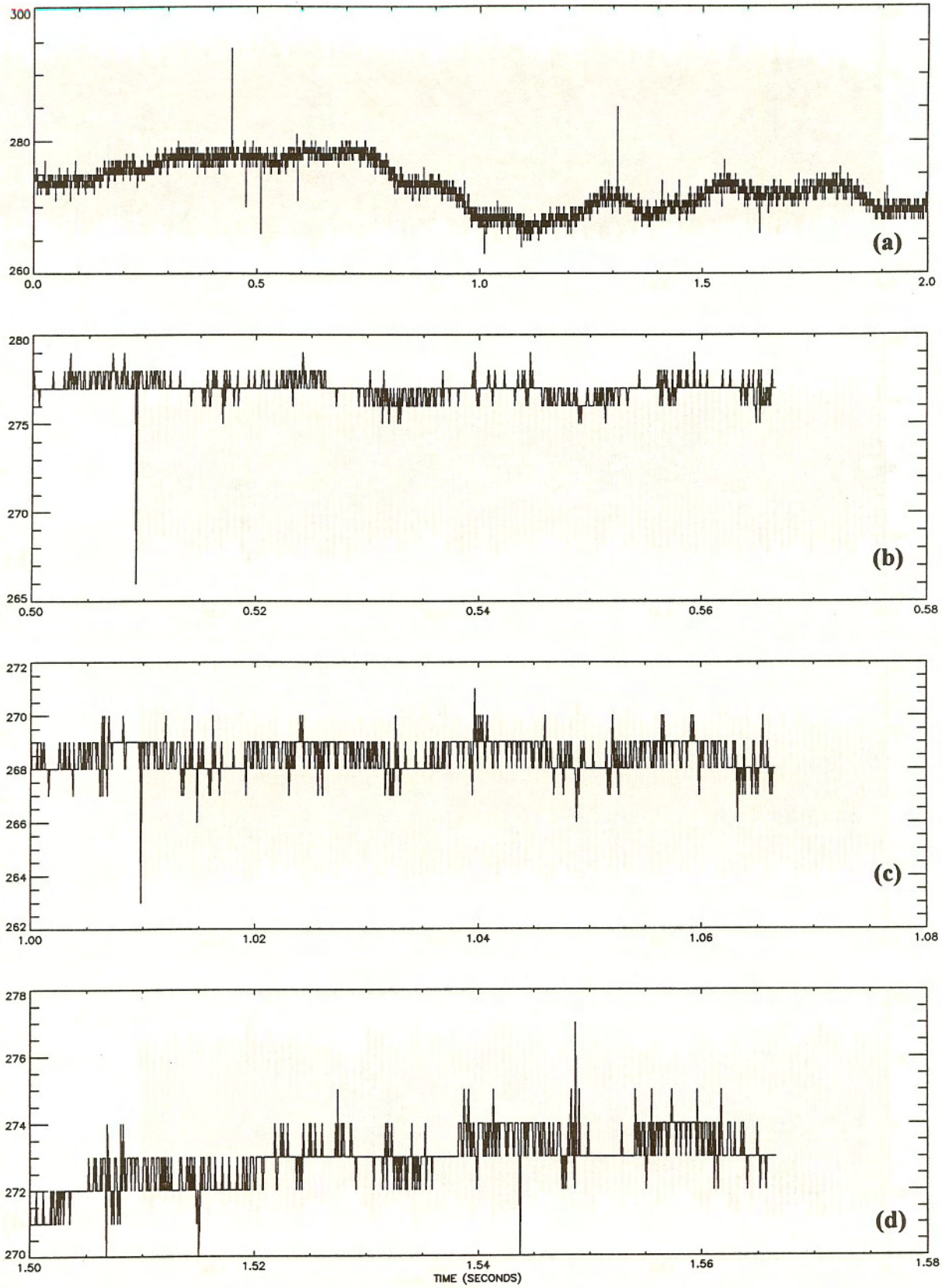

Fig. 2.4. Typical time-serial plots of the first motor current component in the non-chatter regime from (a) 0 - 2s, and expanded plots starting at (b) 0.5s, (c) 1.0s, and (d) 1.5 s.

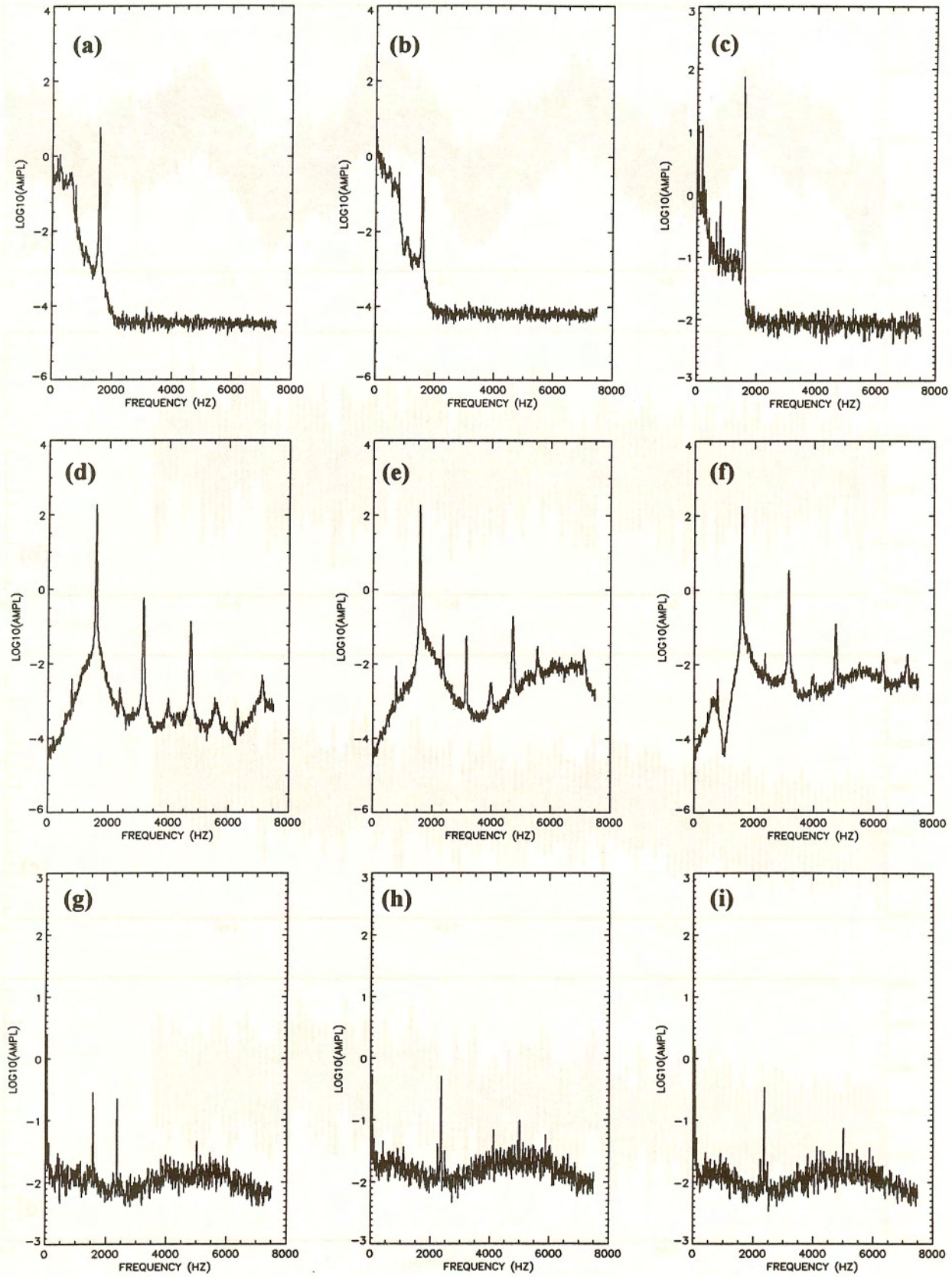

Fig. 2.5. Fourier power spectra for the nine non-chatter data channels: (a) F_x, (b) F_y, (c) F_z, (d) A_x, (e) A_y, (f) A_z, (g) I_1, (h) I_2, and (i) I_3.

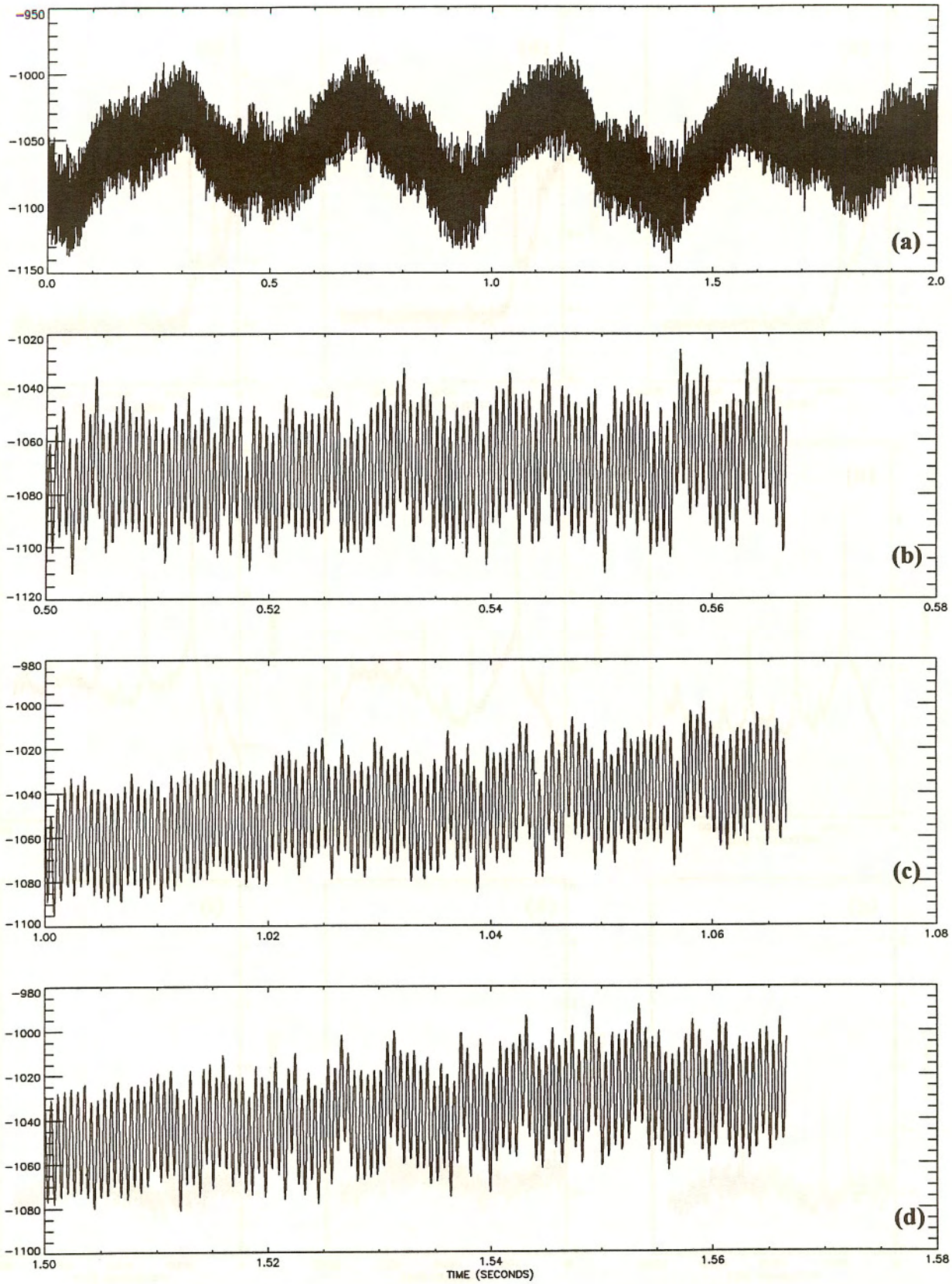

Fig. 2.6. Typical time-serial plots of the y-component of force in the chatter regime from (a) 0 - 2s, and expanded plots starting at (b) 0.5s, (c) 1.0s, and (d) 1.5 s.

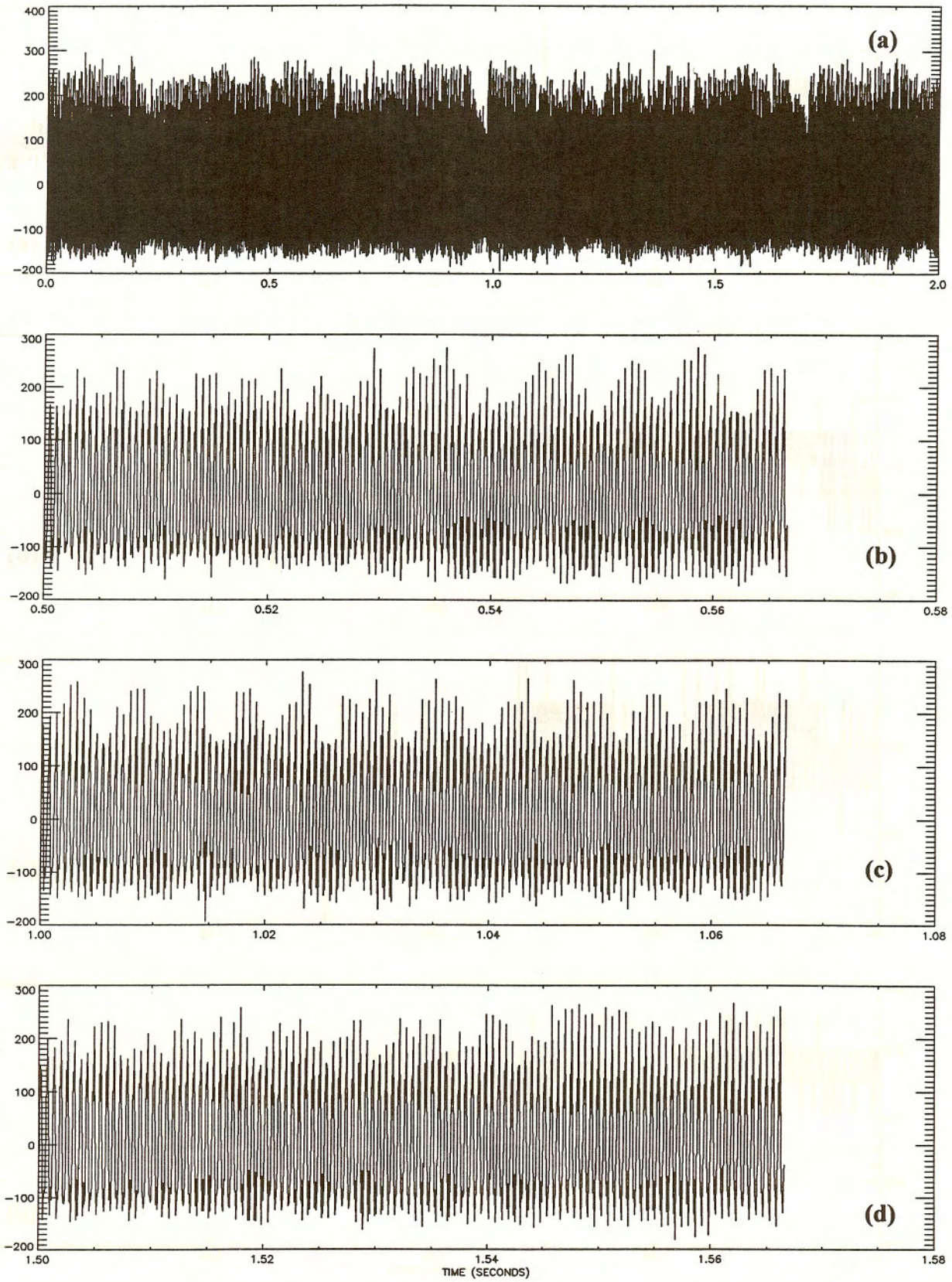

Fig. 2.7. Typical time-serial plots of the z-component of acceleration in the chatter regime from (a) 0 - 2s, and expanded plots starting at (b) 0.5s, (c) 1.0s, and (d) 1.5 s.

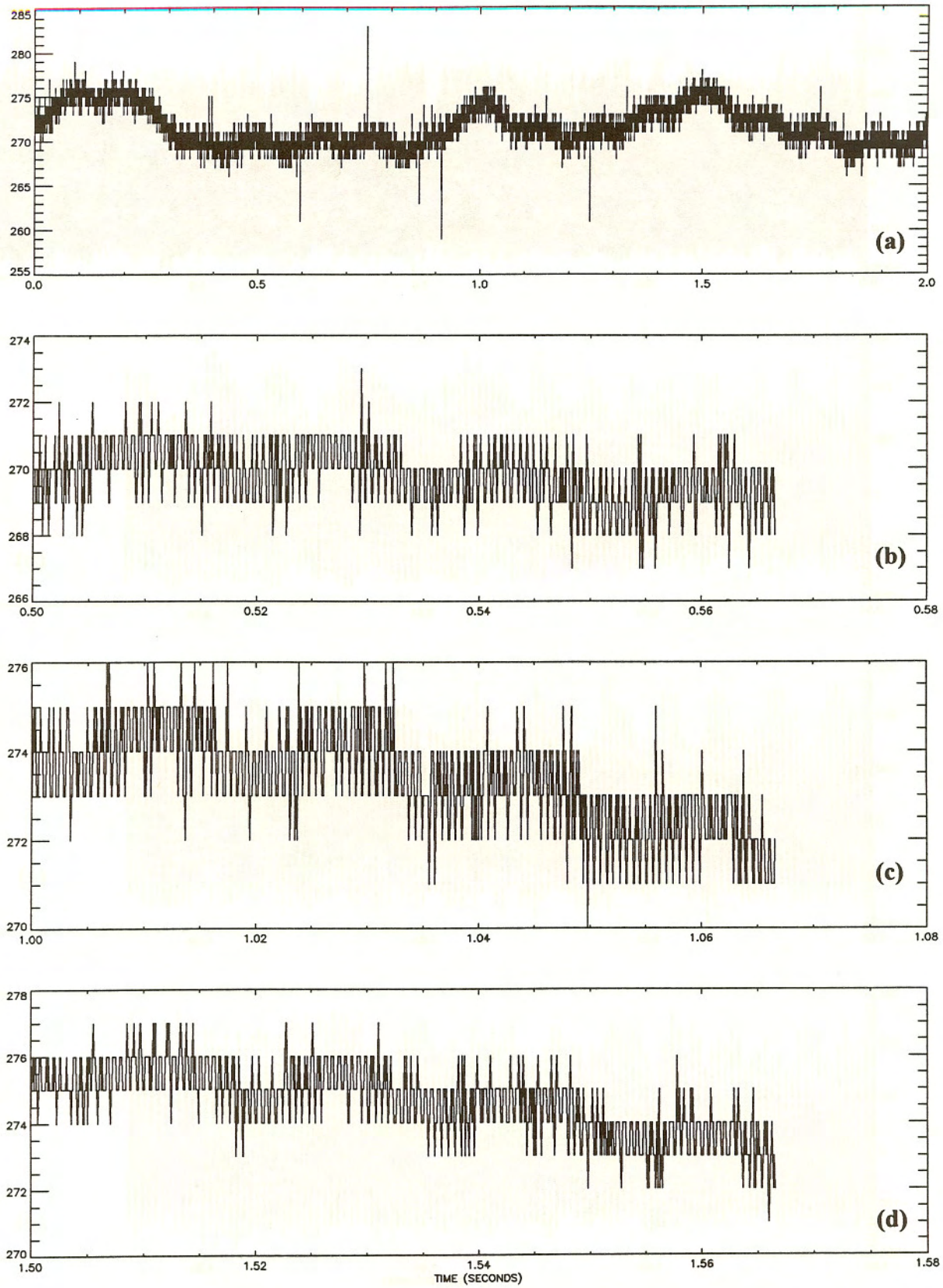

Fig. 2.8. Typical time-serial plots of the first motor current component in the chatter regime from (a) 0 - 2s, and expanded plots starting at (b) 0.5s, (c) 1.0s, and (d) 1.5 s.

The data acquisition digitization capacity was limited to ≤150,000 samples/second. Based on the above results, we eliminated all channels of the force and motor current data, and sampled the three acceleration channels at 50 kilohertz, consistent with the digitization constraint. We obtained five datasets at fixed machining parameters (0.012-inch feed rate per revolution, 0.010-inch depth of cut), while varying the spindle speed (75, 100, 125, and 150 RPM). Figures 2.9-2.11 show typical time-serial plots of A_x (Fig. 2.9), A_y (Fig. 2.10), and A_z (Fig. 2.11).

Several features in the three components of acceleration are noteworthy in these figures.
- The signals are least periodic and the most complex at the lowest spindle speed (75 RPM).
- The complexity decreases and the periodicity increases as the spindle speed increases.
- The signals are most periodic and least complex at the highest spindle speed (150 RPM).

These figures also display distinctions among acceleration components. The dominant frequency in A_z (feed direction) is twice that of A_x (cutting direction) and A_y (tool axis), implying that the effective stiffness in the feed direction is much different from the other two directions. Low (high) A_y values accompany non-chatter (chatter) dynamics, but A_x and A_z show no such trends. Thus, all three spatial directions are important, implying that a chatter model needs to account for dynamics in all three spatial dimensions.

Figures 2.12-2.14 show Fourier power spectra of the three acceleration components, for the four spindle speeds. The spectra for the x- and y-accelerations are very similar, with close correspondence between the amplitude and position of the peaks and valleys. The principal peak in frequency (f_p) for A_x and A_y occurs at 1500-1600 Hertz, but f_p for A_z occurs at 3000-3100 Hertz. Subsequent analysis elucidates this difference.

The Fourier power spectra at the lowest spindle speed (75 RPM) show a series of central peaks with prominent peaks on both sides of the central peak. The difference between the side-band frequencies and the central frequency corresponds to the lowest frequency peak at 200-250 Hertz. We conjecture that this low-frequency peak arises because the lathe controller had difficulty in maintaining a constant spindle speed below 100 RPM. The amplitude of the low-frequency peak (due to the lathe controller) decreases at higher spindle speed, and is insignificant (more than three orders of magnitude below the principal peak) at >100 RPM.

The side-band peaks also are insignificant at the higher spindle speeds, leaving a very clear series of peaks at the principal frequency and multiples (and half-multiples) thereof. No clear peaks appear in the spectra at 75 RPM above 13 kilohertz. However, clear spectral peaks occur over the entire frequency range at higher spindle speeds.

The lathe operator clearly heard chatter at 150 RPM (when the peaks were cleanest), and our results (discussed below) strongly suggest lower chatter levels at 125 RPM (when the peaks were almost as clean). We hypothesize that chatter occurs when a single frequency (with multiples and half-multiples) is dominant (high periodicity and low complexity) at high spindle speed. Conversely, chatter does not occur when many disparate frequencies (high complexity and low periodicity) are present at low spindle speed. If our hypothesis is correct, then chaos tends to suppress chatter, whereas strong periodicity tends to enhance it.

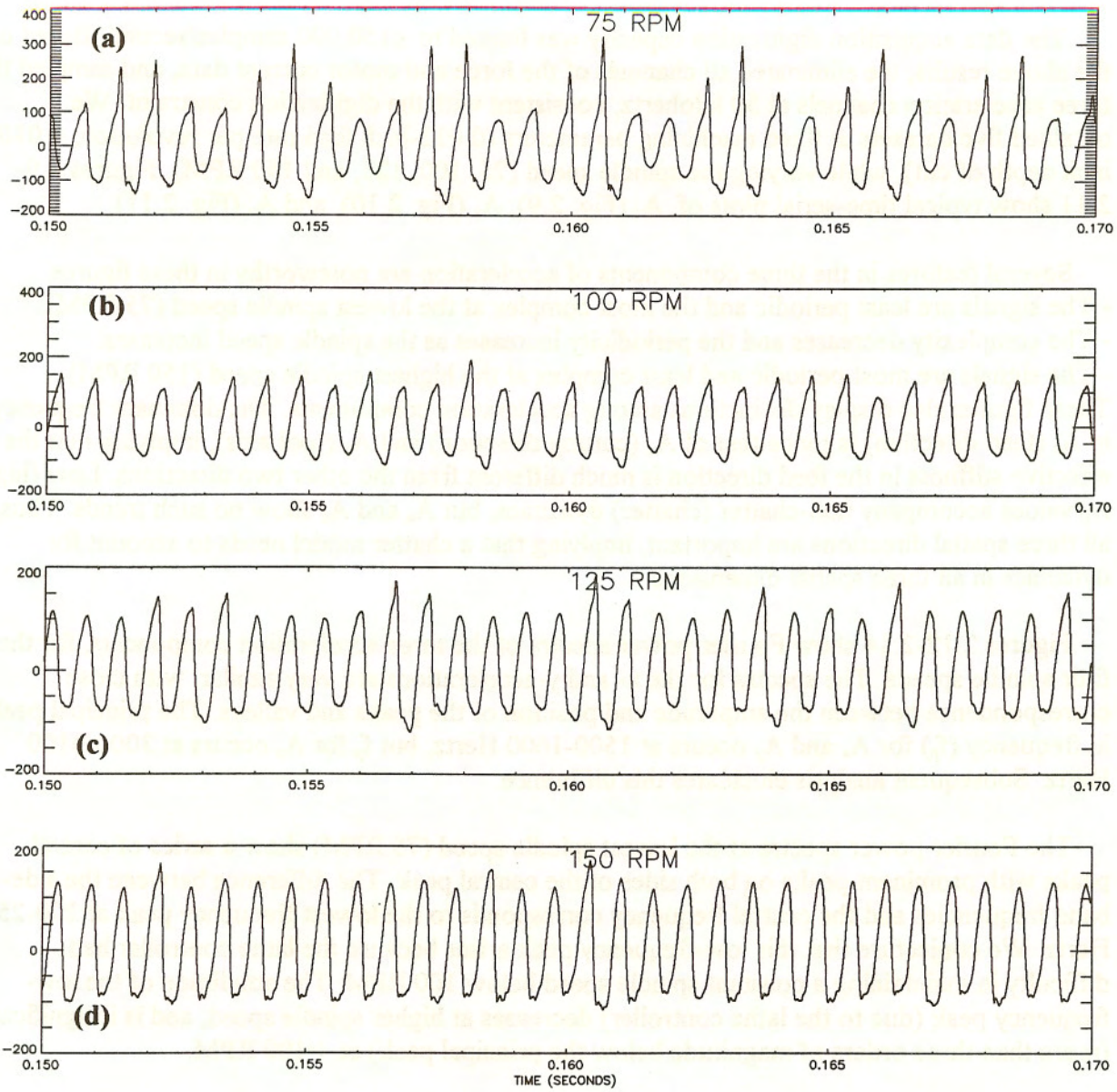

Fig. 2.9. Typical time-serial plots of the x-component of acceleration for (a) 75 RPM, (b) 100 RPM, (c) 125 RPM, and (d) 150 RPM.

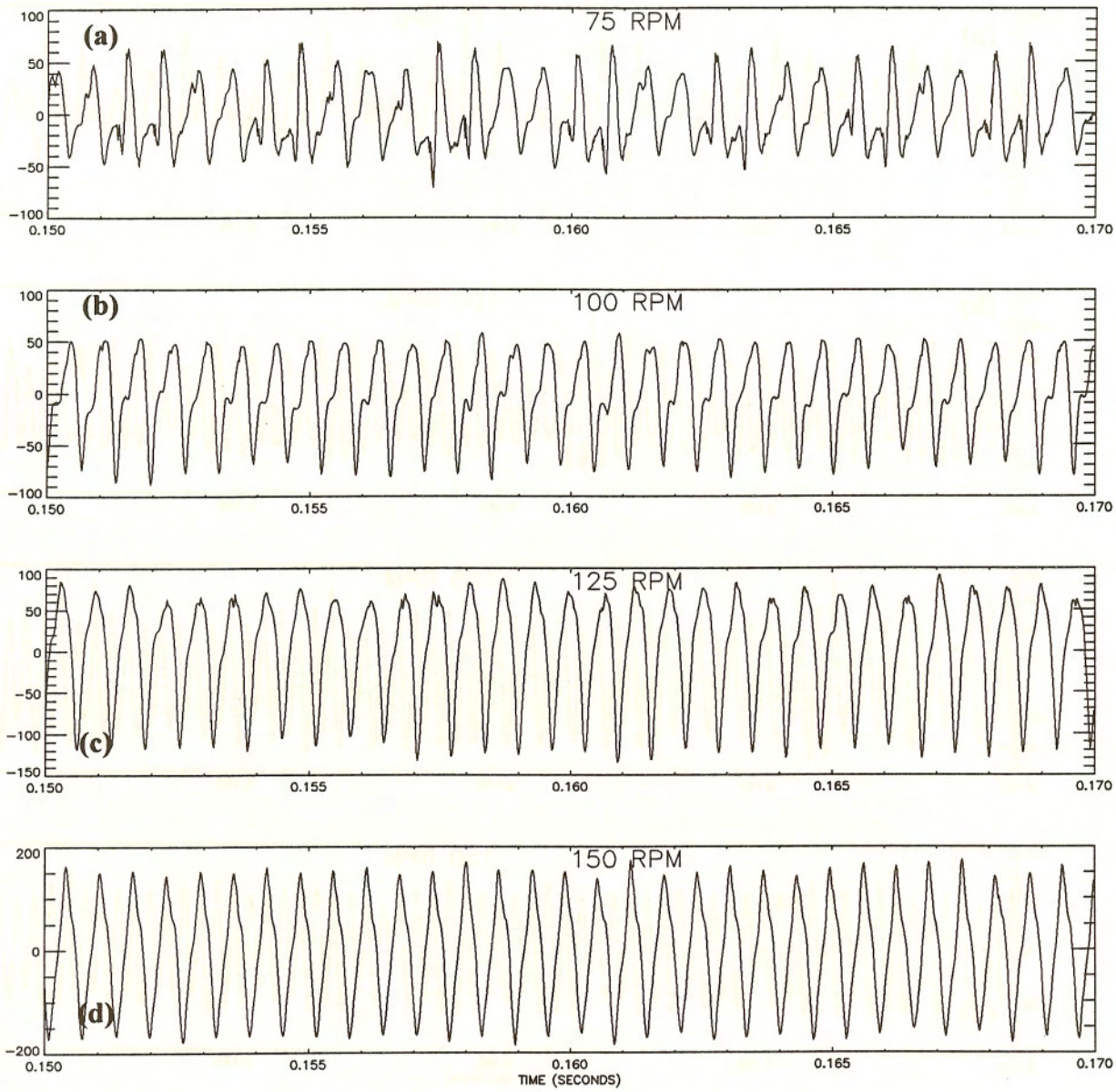

Fig. 2.10. Typical time-serial plots of the y-component of acceleration for (a) 75 RPM, (b) 100 RPM, (c) 125 RPM, and (d) 150 RPM.

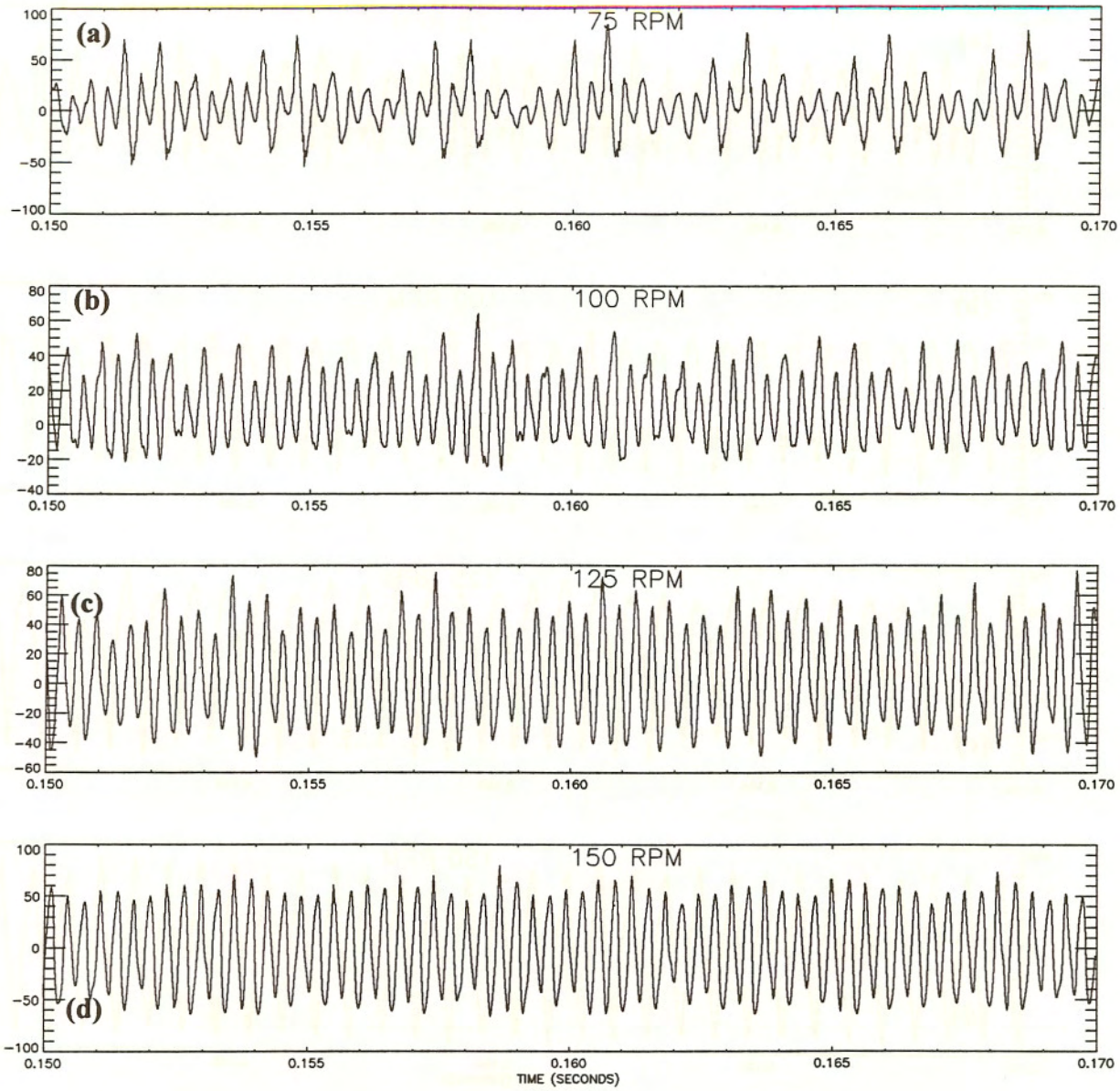

Fig. 2.11. Typical time-serial plots of the z-component of acceleration for (a) 75 RPM, (b) 100 RPM, (c) 125 RPM, and (d) 150 RPM.

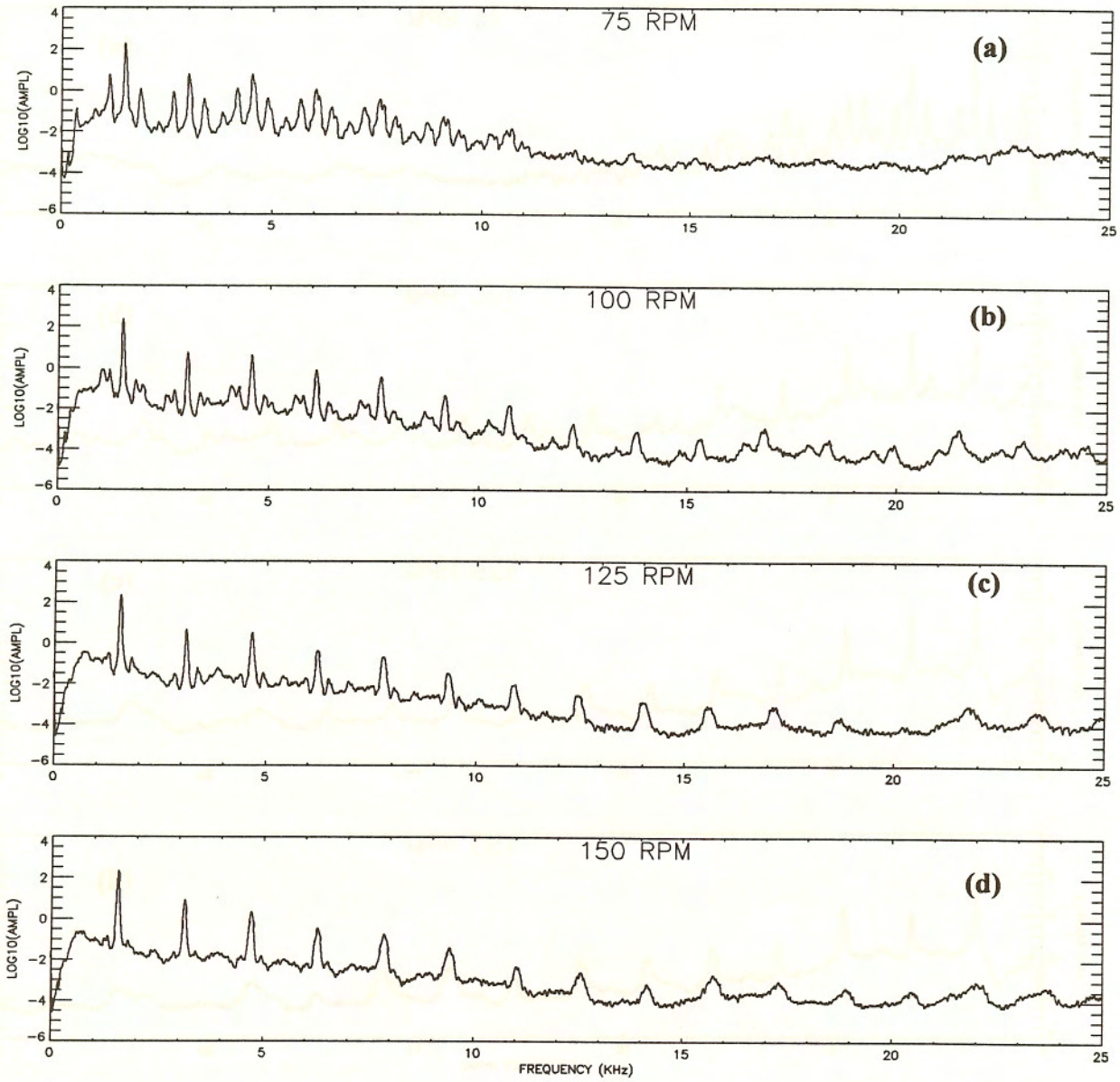

Fig. 2.12. Fourier power spectra (Fourier amplitude versus frequency) of the x-component of acceleration for (a) 75 RPM, (b) 100 RPM, (c) 125 RPM, and (d) 150 RPM.

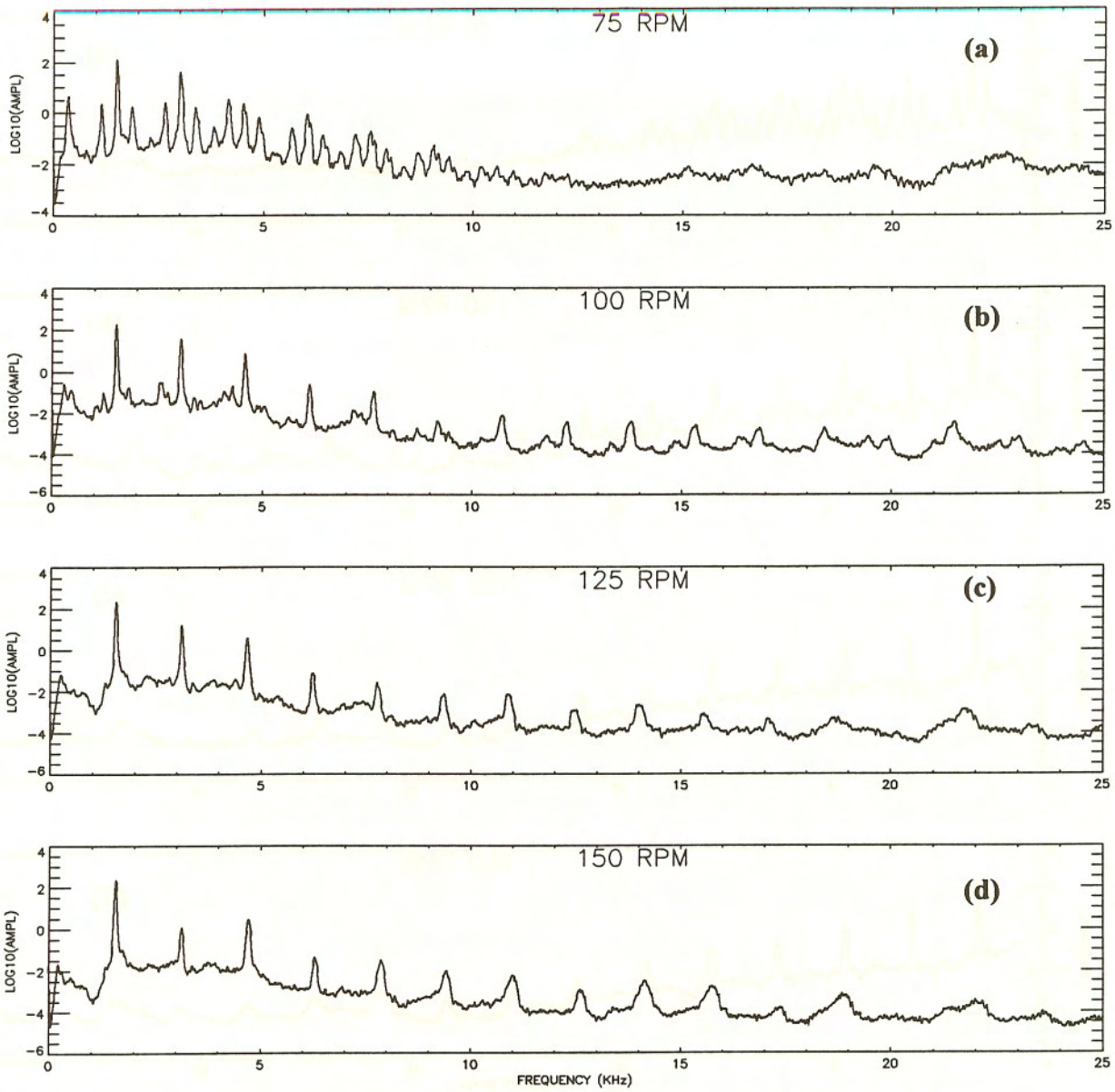

Fig. 2.13. Fourier power spectra (Fourier amplitude versus frequency) of the y-component of acceleration for (a) 75 RPM, (b) 100 RPM, (c) 125 RPM, and (d) 150 RPM.

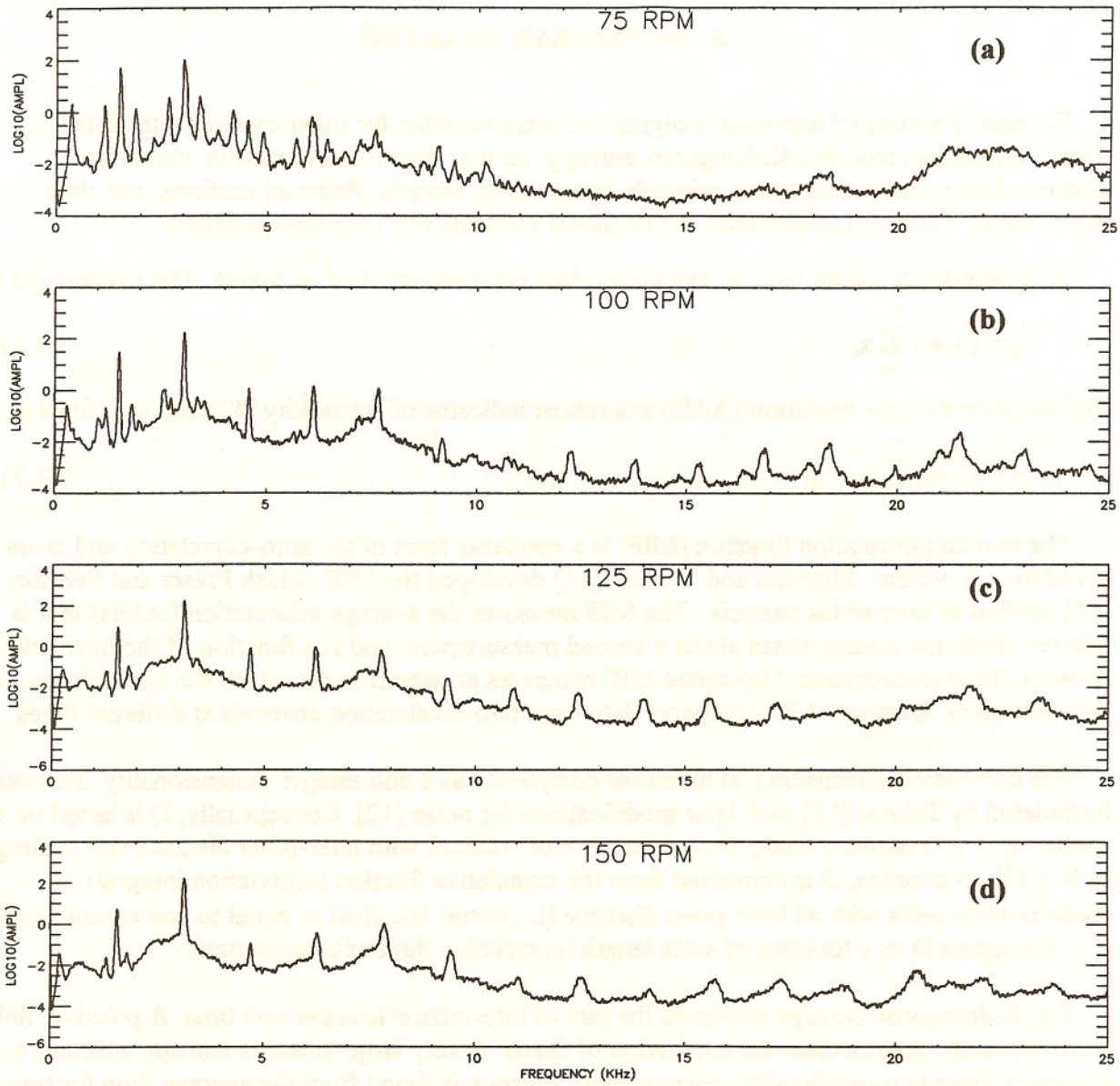

Fig. 2.14. Fourier power spectra (Fourier amplitude versus frequency) of the z-component of acceleration for (a) 75 RPM, (b) 100 RPM, (c) 125 RPM, and (d) 150 RPM.

3. NONLINEAR ANALYSIS

We used a variety of nonlinear analyses that were valuable for other experimental data [11]. These techniques included Kolmogorov entropy, mutual information function, maximum likelihood correlation dimension, principle components analysis, Poincaré sections, and time return maps. This section discusses the nonlinear methods and their interpretation.

The time-serial values (x_i) of machining data are a sequence of w points. The average ($\underline{x}$) is:

$$\underline{x} = (1/w) \sum_{i=1}^{w} x_i \tag{3.1}$$

The absolute average deviation (AAD) is a robust indicator of variability [12] and is defined as:

$$a = (1/w) \sum_{i=1}^{w} |x_i - \underline{x}| \tag{3.2}$$

The mutual information function (MIF) is a nonlinear form of the auto-correlation and cross-correlation functions. Shannon and Weaver [13] developed the MIF, which Fraser and Swinney [14] applied to time series analysis.. The MIF measures the average information (in bits) that is inferred from one measurement about a second measurement, and is a function of the time delay between the measurements. Univariate MIF compares acceleration data from the same channel at different times. Bivariate MIF compares data from two acceleration channels at different times.

The correlation dimension (D) measures complexity as a non-integer dimensionality, and was formulated by Takens [15] with later modifications for noise [12]. Conceptually, D is based on the number (N) of random-point-pairs (as measure of volume) with inter-point distance (L), scaling as $N \propto L^D$. In practice, D is computed from the cumulative fraction (correlation integral) of random-point-pairs with an inter-point distance (L_∞ norm) less than or equal to some scale length (L). We report D as a function of scale length (correlation dimension spectrum).

The Kolmogorov entropy measures the rate of information loss per unit time. A positive, finite entropy usually gives a clear demonstration of chaos. A very large, positive entropy indicates a stochastic (totally unpredictable) phenomenon. Entropy is found from the average time for two points on an attractor to go from an initial separation (e.g., $L < a$), to become separated by more than a specific distance (e.g., $L \geq a$). We use the maximum-likelihood entropy from the method by Schouten, Takens, and van den Bleek [16], also called the order-2 Kolmogorov entropy which hereafter we call simply "entropy." We report K as a function of scale length (entropy spectrum).

The entropy (K) and correlation dimension (D) usually are reported in the limit of zero scale length. However, experimental data have noise and finite measurement precision. Consequently, we report K and D spectra for a range of scale lengths, with small scale length corresponding to noise (typically for $L \leq a$), and larger scale length (typically for $L \geq 5a$) spanning more global dynamics. These spectra do not capture the full dynamic complexity, i.e., their values are smaller than expected for the zero-scale-length limit. Rather, we interpret K and D spectra as nonlinear measures of the finite-scale dynamics, because the zero-scale-length limit is unattainable due to noise and finite measurement precision.

Principal component analysis reconstructs the nonlinear dynamics from experimental data. Abarbanel et al. [17] and Grassberger et al. [18] review this and related techniques. A sequence of data (x_i) is measured at equal intervals (τ), beginning at some initial time (t_0), $x_i = x(t_0 + i\tau)$. Conversion of this data to a system of differential equations for the dynamics requires that the derivatives be approximated by finite differences of the data values [$dx/dt = (x_{i+1} - x_i)/\tau$, $d^2x/dt^2 = (x_{i+2} - 2x_{i+1} - x_i)/\tau^2$, etc.]. These and higher derivatives add to the information that already resides in the x_i measurements, as multiples of other measurements at times that are multiples of the observation interval (τ). Thus, a more direct method [19] relies on the use of lagged variables, $x_{n+i\lambda} = x(t_0 + (n+i\lambda)\tau)$, with λ as an integer lag that is determined from the data. In particular, this method uses a collection of time lags to create a vector of data in d dimensions:

$$y(n) = [x_n, x_{n+\lambda}, x_{n+2\lambda}, \ldots, x_{n+(d-1)\lambda}] \tag{3.3}$$

Takens [20] found that faithful reconstruction of the system dynamics requires the embedding dimension (d) to be at least one plus twice the number of degrees of freedom (DOF). We measure the DOF for a given scale length as the correlation dimension (D), yielding an embedding dimension of $d \geq 2D + 1$. If the lag value is too small, then adjacent coordinates, $x_{n+j\lambda}$ and $x_{n+(j+1)\lambda}$, will be so close together in numerical value that they cannot be distinguished. If the lag value is too large, then these same adjacent coordinates are essentially independent due to the inherent unpredictability of chaotic systems after a long time. An optimal time length [14] should span enough data to go from the first maximum in the univariate MIF (maximum nonlinear correlation that always occurs at zero lag) to the first minimum in the MIF (minimum nonlinear correlation at M_1 as measured in timesteps). The vector in Eq. 3.3 has a total of (d-1) λ timesteps, so the lag value is obtained from $M_1 = (d-1)\lambda \geq (2D + 1 - 1)\lambda = 2D\lambda$, or $\lambda \leq M_1/2D$. Broomhead and King [21] obtained the eigenvalues (σ_i) of the covariance matrix of y(n), which are all positive and can be ordered monotonically from largest to smallest. The larger eigenvalues correspond to the true system dynamics in d_T dimensions and typically constitute ≥99% of the sum over all the eigenvalues. Other eigenvalues arise from noise in d_N dimensions with $d = d_T + d_N$, corresponding to a noise floor in σ_i versus i. The eigenvectors are orthogonal and are used to project out the independent dynamic components from the data, e.g., $z_k(i)$ as the k-th dynamic component at the i-th timestep. The "principal components" match the larger eigenvalues. The system dynamics are visualized in two- or three-dimensions by connecting the sequence of points ($z_1(i)$, $z_2(i)$) for the first two principal components, or by connecting the triplet ($z_1(i)$, $z_2(i)$, $z_3(i)$) for the first three principal components. When the above constraints are satisfied, Takens' embedding theorem [20] guarantees that the resulting representation faithfully reconstructs the system dynamics.

The machining data consists of multiple data channels, so the principal component analysis can be applied to each channel. The dynamics can be reconstructed geometrically by connecting the time sequence of three orthogonal acceleration values (A_x, A_y, A_z). Another visualization technique involves the intersection of the line that connects the sequence of values (A_x, A_y, A_z) at each time with the plane A_i=0, for i = (x, y, or z). This set of two-dimensional points for the system dynamics passing from A_i <0 to A_i >0 is called a positive-going puncture plot (or Poincaré section). A negative-going Poincaré section shows system motion that goes from A_i >0 to A_i <0, The two Poincaré sections are not the same because in one direction the motion is constrained by contact with the part but in the other direction the motion has no such constraint.

4. RESULTS AND DISCUSSION

We obtained five datasets for stainless steel machining (0.012-inch feed rate per revolution, 0.010-inch depth of cut), at four spindle speeds (75, 100, 125, and 150 RPM), as summarized in Table 4.1. Datasets #091802 and #091803 are at the same spindle speed (100 RPM), showing consistency between different datasets for the same parameters; other nonlinear measures (not shown) demonstrate the same consistency. The principal peak frequency (f_p) in the Fourier spectra increases monotonically with spindle speed for all three acceleration channels. The number of timesteps per cycle (T_c) measures the average cycle period. $T_c(A_x)$ and $T_c(A_z)$ decrease slowly with increasing spindle speed, but $T_c(A_y)$ is non-monotonic. The acceleration amplitude range (ΔA_i) is the difference between the largest and smallest value of A_i. We note that ΔA_y rises monotonically as the spindle speed increases, with the two largest values corresponding to the chatter regime. The amplitude range in the other two channels (ΔA_x and ΔA_z) is non-monotonic.

Table 4.1 Summary of analysis results

	Dataset				
Parameter	091801	091802	091803	091804	091805
Spindle speed (RPM)	75	100	100	125	150
$f_p(A_x)$ (Hertz)	1514	1526	1538	1563	1575
$f_p(A_y)$ (Hertz)	1514	1526	1538	1563	1575
$f_p(A_z)$ (Hertz)	3027	3064	3064	3113	3149
$T_c(A_x)$ (timesteps/cycle)	33.0	32.7	32.6	32.1	31.7
$T_c(A_y)$ (timesteps/cycle)	26.2	27.3	30.7	32.1	31.7
$T_c(A_z)$ (timesteps/cycle)	16.5	16.3	16.3	16.0	15.9
ΔA_x (arbitrary units)	584	479	433	474	387
ΔA_y (arbitrary units)	169	219	178	272	387
ΔA_z (arbitrary units)	172	154	115	153	178
$M_1(A_x)$ (timesteps)	9	8	8	8	7
$M_1(A_y)$ (timesteps)	4	5	5	6	5
$M_1(A_z)$ (timesteps)	5	4	4	4	4
$D_{min}(A_x)$	2.23	1.87	1.67	1.65	1.58
$D_{min}(A_y)$	2.53	1.60	1.45	1.38	1.41
$D_{min}(A_z)$	2.43	2.38	2.24	1.87*	1.81*
$D_{max}(A_x)$	2.61	2.59	2.37	2.58	2.95
$D_{max}(A_y)$	3.15	2.45	2.36	1.97	1.58
$D_{max}(A_z)$	2.55	2.47	2.26	1.87*	1.81*
$K(A_x)$ (bits/timestep)	0.025	0.015	0.012	0.011	0.0084
$K(A_y)$ (bits/timestep)	0.026	0.0056	0.0052	0.0039	0.0026
$K(A_z)$ (bits/timestep)	0.051	0.032	0.028	0.017	0.013

* Starred values denote that no local minimum or maximum occurred; see text for discussion.

Figure 4.1 shows the univariate MIF for the three acceleration components. From Section 3, the first minimum (M_1) in the MIF measures the time when the signal is least correlated with itself and is the important feature of these results. Table 4.1 shows M_1 for each channel, with $M_1(A_x)$ decreasing slightly with increasing spindle speed, but M_1 for A_y and A_z being roughly constant. The range is $4 \leq M_1$ (timesteps) ≤ 9, implying the chaotic dynamics become unpredictable after 80-180 microseconds. A fully adequate sampling rate would allow $M_1 \geq 10$ timesteps, so the present range indicates that our sampling frequency is only marginally adequate, as constrained by the existing data acquisition system.

Figure 4.2 shows typical correlation dimension (D) spectra and correlation integral. The error bars show the 95% confidence limits for each point. D is large for small values of scale length, corresponding to high complexity (or noise) at short scale length. D decreases to much smaller values at larger scale length, corresponding to global structure. Between these extremes, a plateau region usually appears, which we characterize by the local minimum (D_{min}) and maximum (D_{max}). Table 4.1 shows D_{min} and D_{max} for each acceleration component. The starred (*) values of acceleration for the z-component in Table 4.1 mean that no local minimum or maximum occurred, so these values correspond to the flattest part of the plateau. In all but one case, the values of D_{min} and D_{max} decrease with increasing spindle speed. The exception is $D_{max}(A_x)$, which decreases to a minimum at 100 RPM, then rises with increasing spindle speed (125-150 RPM). Over the full extent of spindle speeds, the range is $1.38 \leq D_{min} \leq 2.53$ and $1.58 \leq D_{max} \leq 3.15$. This range implies that an appropriate set of four simultaneous first-order differential equations can model the essence of the tool-part dynamics for these spindle speeds.

Figure 4.2 also shows typical entropy (K) spectra. The error bars show the 95% confidence limit for each point. K is large for small values of scale length, corresponding to a fast rate of information loss per timestep for noise. K decreases monotonically with increasing scale length, corresponding to progressively less information loss at more global length scales. The K-spectra for A_x and A_y have two domains. For $a \leq L \leq (3\text{-}4)a$, K decreases slowly with increasing scale length, corresponding to local structure in the dynamics. For $(3\text{-}4)a \leq L \leq 7a$, K decreases much more rapidly with an essentially linear slope on these log-linear plots (an exponential decrease with scale length), corresponding to global structure in the dynamics. The K-spectrum for A_z has a more gradual transition in slope, corresponding to different dynamics in the transition for local-to-global structure. Since the plateau region in the D-spectra occurs for a scale length of $1.5a \leq L \leq 4.25a$, we characterize the K-spectra by a typical value at L=2a as shown in Table 4.1. These K-values decrease with increasing spindle speed for all three acceleration channels. This trend is consistent with more (less) complexity and chaotic features, and less (more) periodicity at low (high) spindle speed.

Figure 4.3 illustrates the three-dimensional geometric structure of the machining dynamics by following the time-serial sequence of points, (A_x, A_y, A_z), for many periods. The resulting figure is called an "attractor," representing the global region to which the dynamics is confined. A totally random (stochastic) process forms a compact sphere. This figure shows a clear structure in the attractor, indicative of a deterministic process. At low spindle speed (non-chatter regime), the attractor is an elongated torus with sharp corners. As the spindle speed increases, the toroidal attractor becomes a less elongated and more circular.

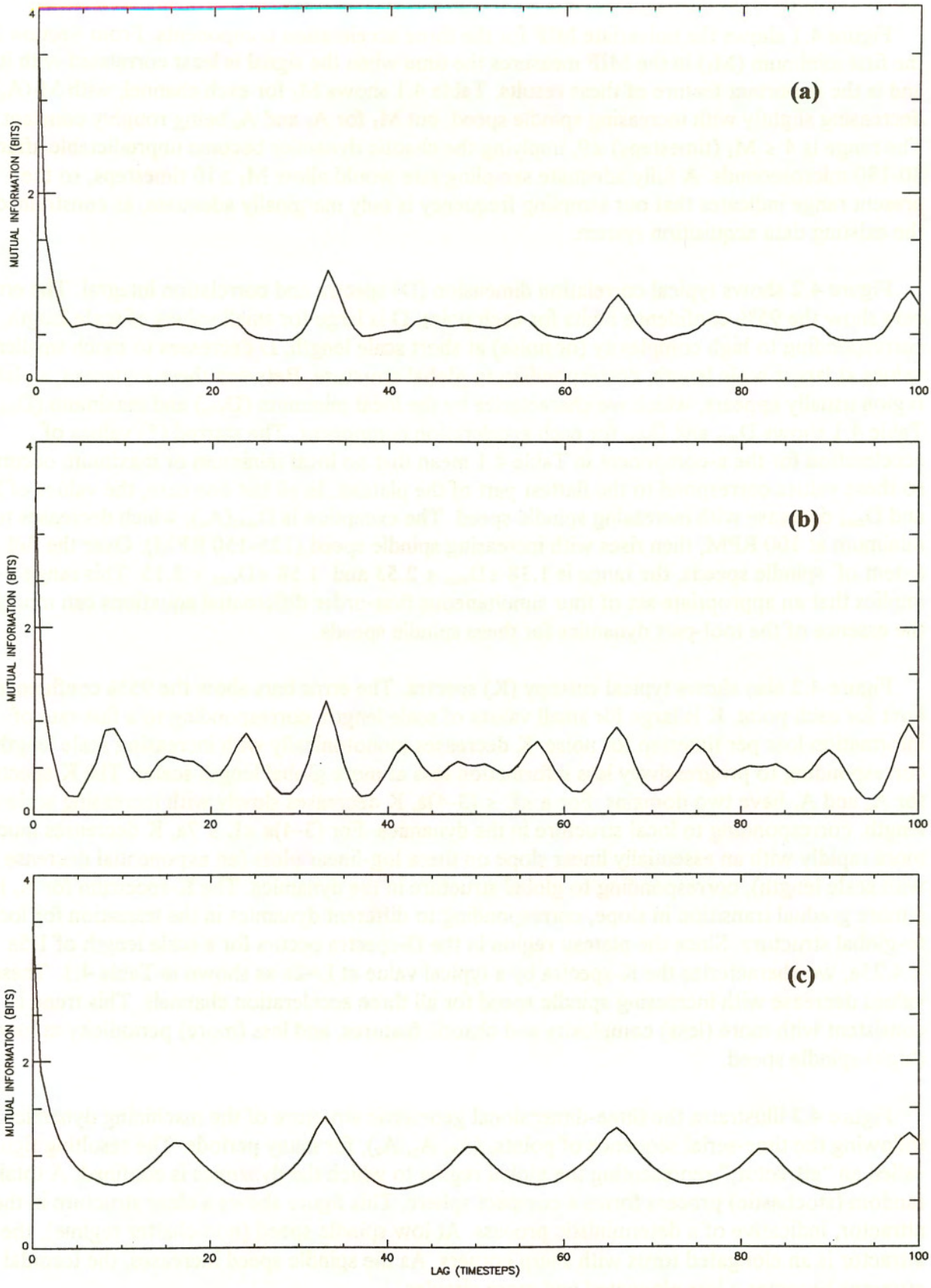

Fig. 4.1. MIF plots of dataset #091801 for (a) A_y, (b) A_z, and (c) A_x versus the time lag.

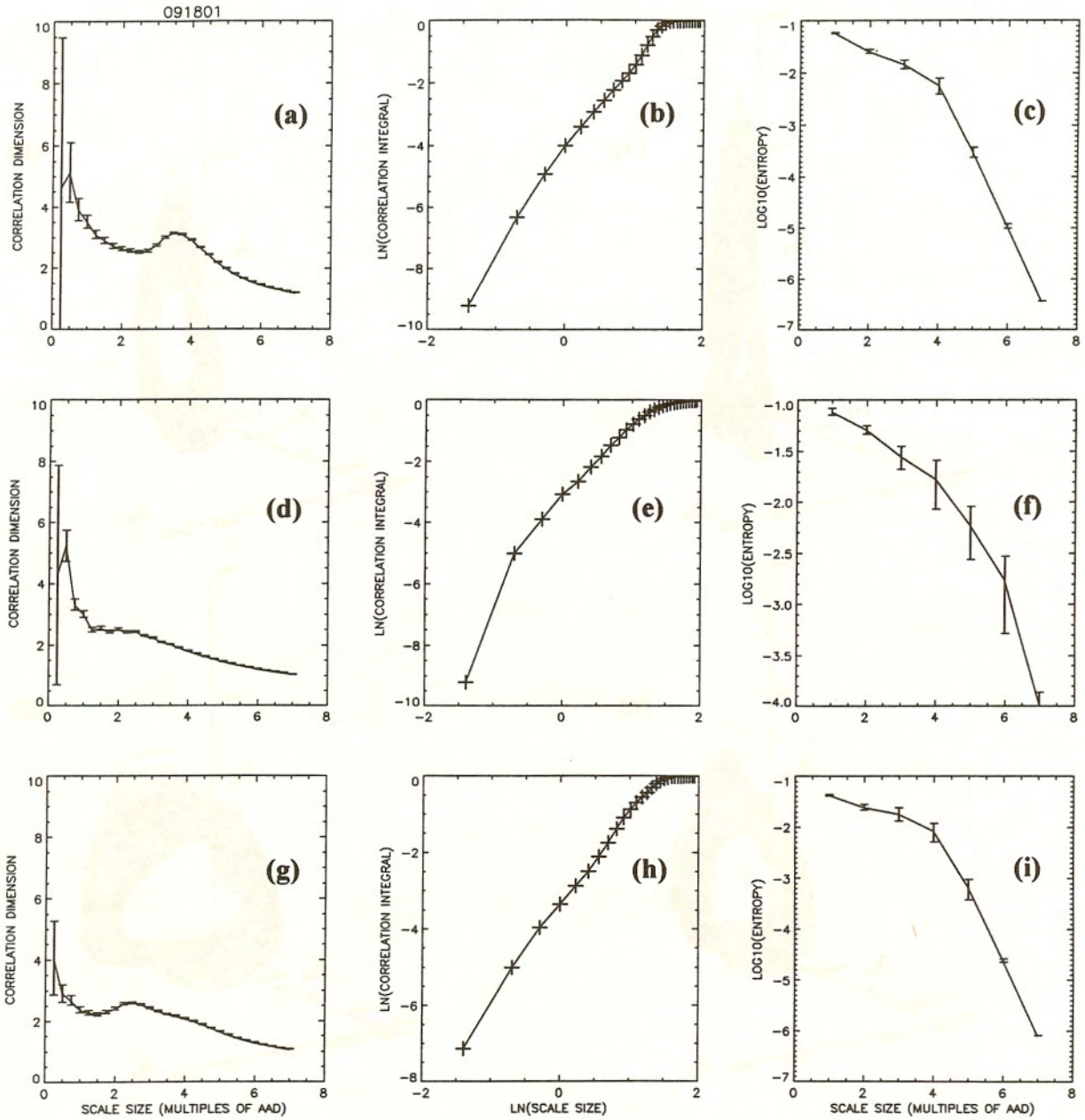

Fig. 4.2. Typical results for dataset #091801: (a) D-spectrum for A_y, (b) correlation integral for A_y, (c) K-spectrum for A_y, (d) D-spectrum for A_z, (e) correlation integral for A_z, (f) K-spectrum for A_z, (g) D-spectrum for A_x, (h) correlation integral for A_x, and (i) K-spectrum for A_x.

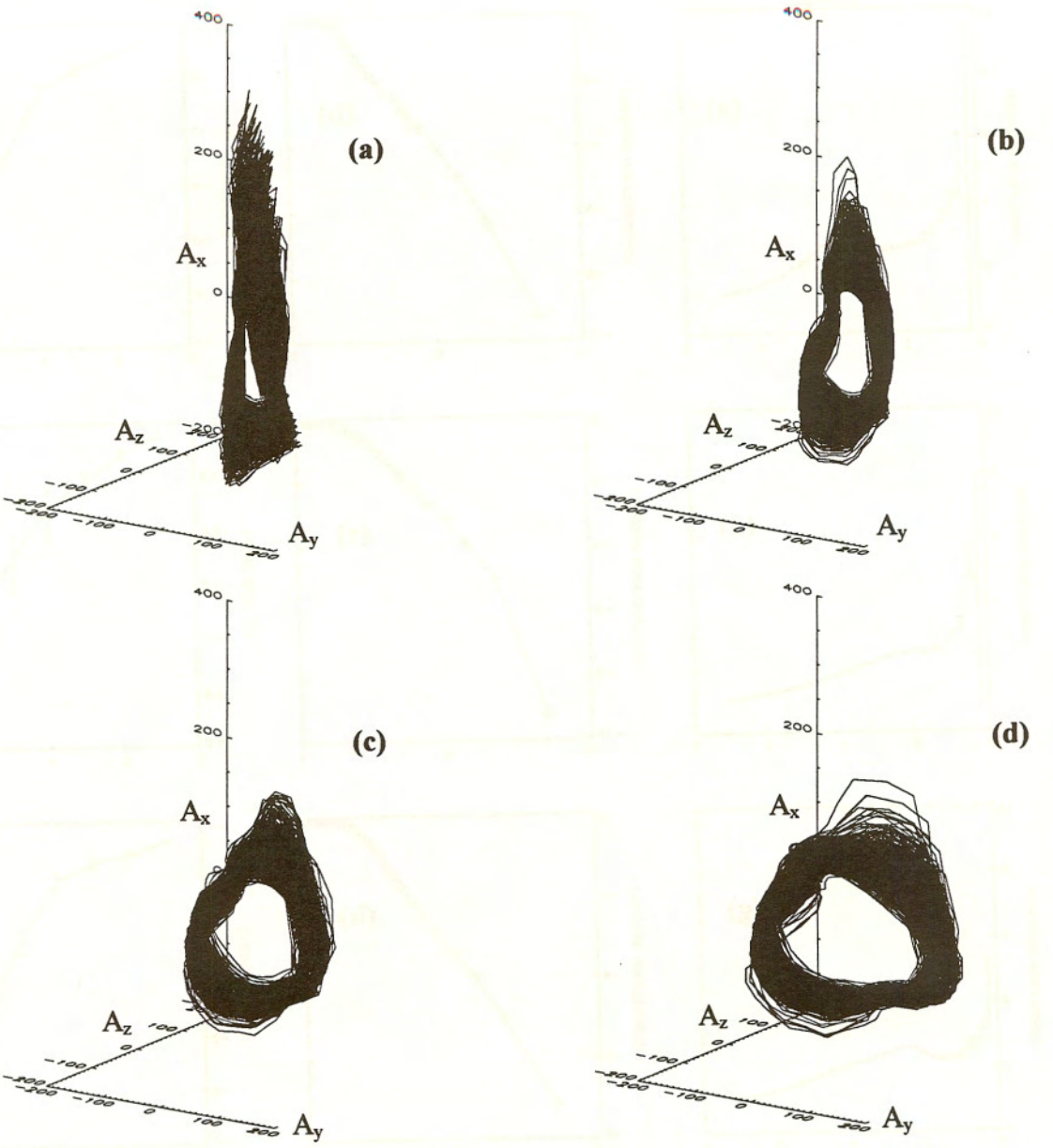

Fig. 4.3. Attractor plots in (A_x, A_y, A_z) space for spindle speeds of (a) 75 RPM, (b) 100 RPM, (c) 125 RPM, and (d) 150 RPM.

Figure 4.4 shows the three-dimensional attractors from principle components analysis. The top row shows plots for dataset #091801 (75 RPM), with #091802 (100 RPM) as the second row from the top, #091803 (100 RPM) as the middle row, #091803 (125 RPM) as the fourth row, and #091805 (150 RPM) as the bottom row. Each column shows one acceleration, (A_y, A_z, A_x) from left to right, respectively. Complex features appear at 75 RPM, with the A_z attractor as a double loop, that is very different from the structure of the other two accelerations. As the spindle speed rises, this double loop in the A_z attractor becomes a cylinder (moving down the center column). The dynamics in A_x and A_y are also less complex at higher speed.

Figures 4.5-4.6 show positive- and negative-going Poincaré sections for $A_x = 0$, respectively. Each Poincaré section is a single cluster of points. The positive-going section at 75 RPM (Fig. 4.5a) is a dense elongated cluster about a line with negative slope. The clusters at 100 RPM (Figs. 4.5b-c) are slightly elongated and have no clear orientation. The clusters at 125-150 RPM (Figs 4.5d-e) are more elongated with no A_y values close to zero (which the other subplot do have) and with a nearly vertical orientation. The negative-going sections (Fig. 4.6) form clusters about a line with negative slope, and become less elongated as the spindle speed rises. The clusters at 125-150 RPM (Fig. 4.6d-e) have a nearly vertical orientation.

Figure 4.7 shows positive-going Poincaré sections for $A_z = 0$. Each Poincaré section has two compact clusters, indicating double loops in the dynamics (at twice the principal frequency of A_x and A_y). The clusters change shape and orientation as the spindle speed increases. The upper clusters ($A_x > 0$) span $A_y = 0$ for non-chatter cutting (subplots-a, -b, -c), but during chatter, upper clusters occur only for $A_y > 0$ (subplots-d and -e). The lower cluster ($A_x < 0$) is very elongated at 75 RPM (subplot-a) and oriented along a line with nearly vertical (negative) slope. The lower cluster is less elongated at 100 RPM and oriented along a line with a nearly vertical (positive) slope. The lower clusters are slightly elongated at 125-150 RPM. The line between the centroids of the two clusters has a positive slope that decreases as the spindle speed rises.

Figure 4.8 shows negative-going Poincaré sections for $A_z = 0$. These sections also display pairs of compact clusters. The upper cluster occurs in the quadrant with $A_x > 0$ and $A_y < 0$; the lower cluster appears in the quadrant with $A_x < 0$ and $A_y > 0$. The most significant difference among these sections appears at 150 RPM (subplot-e) which shows the upper cluster with larger-magnitude A_y-values and more elongation than the other clusters.

Figure 4.9 shows positive-going Poincaré sections for $A_y = 0$. The sections at low speed (subplots-a and -b) show two clusters of points (one for $A_x > 0$ and the other for $A_x < 0$), indicating double loops in dynamics that are not apparent from the attractors in Figs. 4.3-4.4. Only a single, compact cluster occurs for $A_x > 0$ at high spindle speeds (subplots-d and -e). The elongated cluster for dataset #091803 (subplot-c) has a few scattered points in the right portion of the plot, where the second cluster appeared in subplots-a and -b. We note that at the completion of dataset #091802, the tool ran off the end of the cylindrical workpiece. Dataset #091803 began at the other end of the cylindrical part at a diameter that was smaller by twice the cutting depth (2 x 0.01 inch), corresponding to a diameter change ~1%. This unintentional percent-level change in machining parameters allowed us to record what seems to be a clear transition from the non-chatter to the chatter regime.

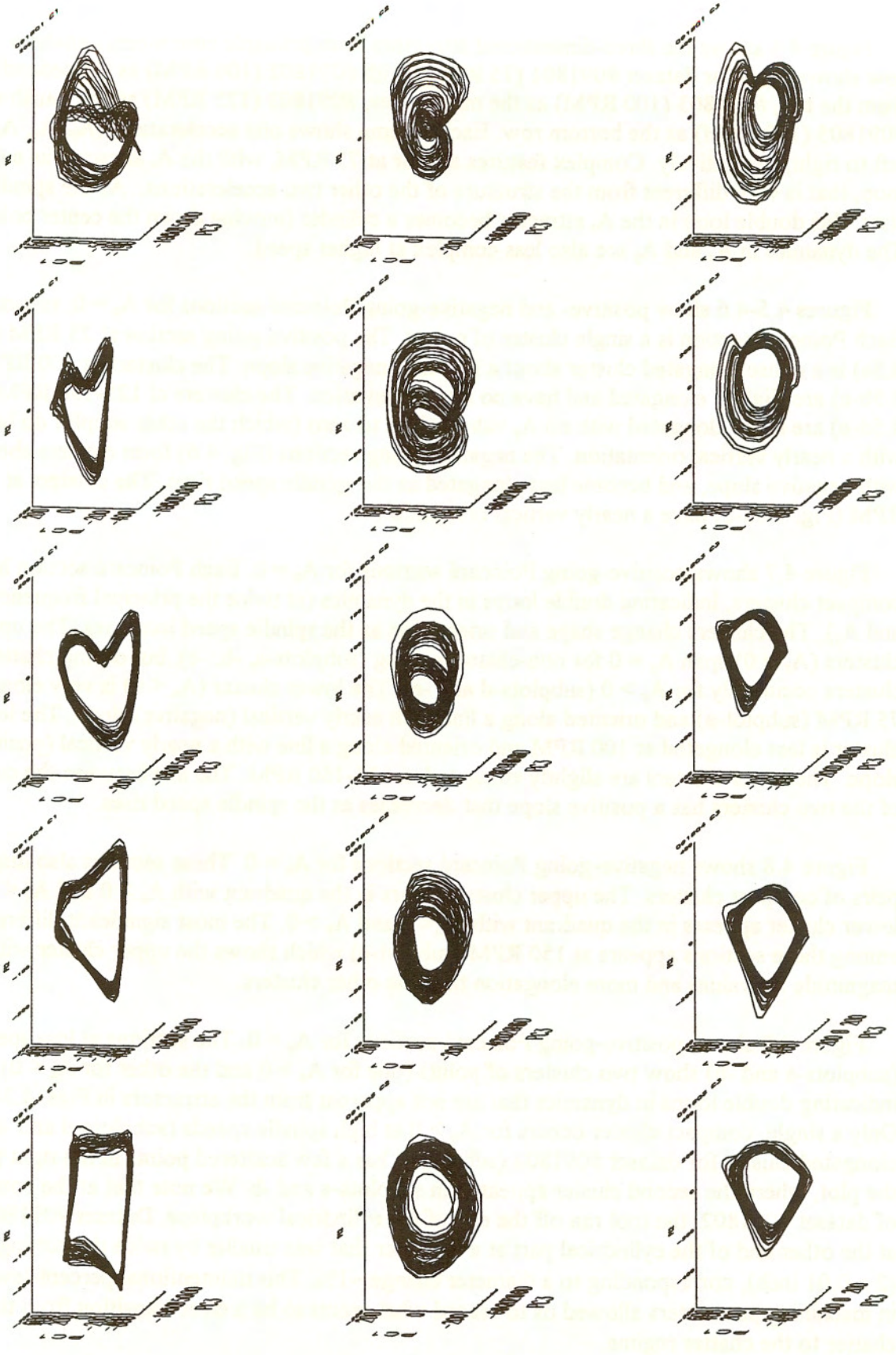

Fig. 4.4. Attractor plots from principal components analysis for each dataset (rows) and for each acceleration channel (columns). See text for identification of plots and discussion.

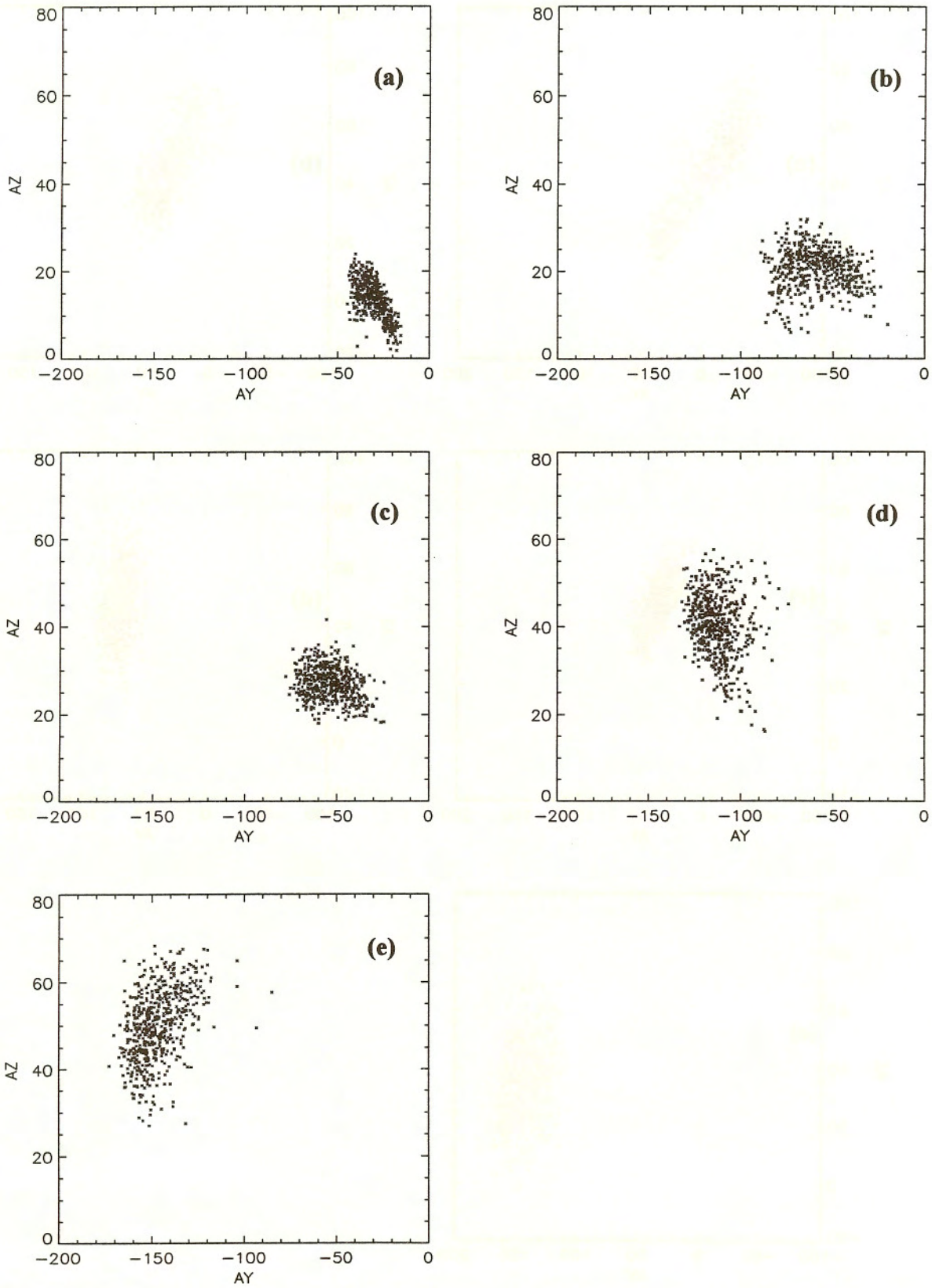

Fig. 4.5. Positive-going Poincaré sections for $A_x = 0$: (a) 75 RPM, (b) 100 RPM (dataset #091802), (c) 100 RPM (dataset #091803), (d) 125 RPM, (e) 150 RPM.

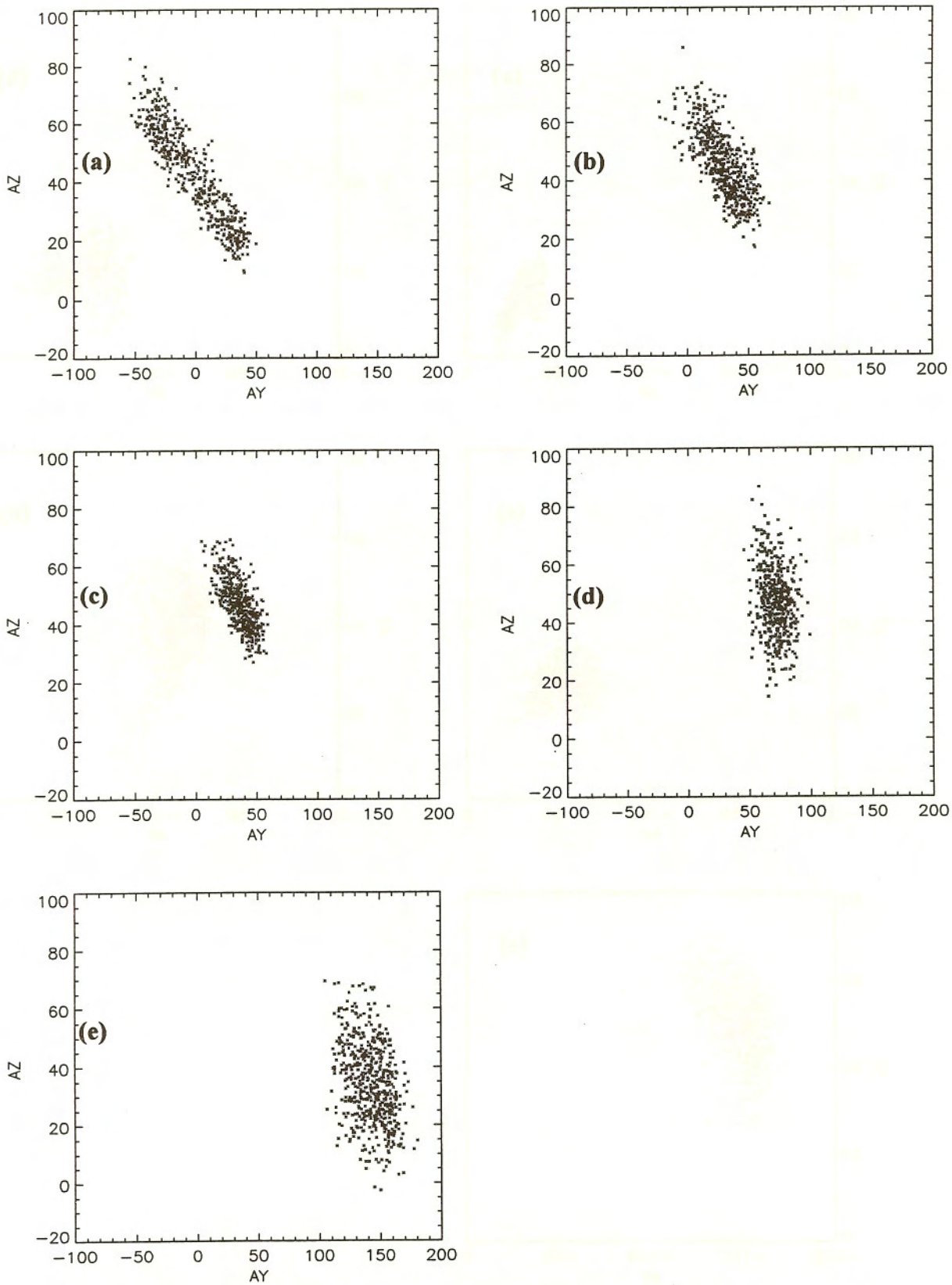

Fig. 4.6. Negative-going Poincaré sections for $A_x = 0$: (a) 75 RPM, (b) 100 RPM (dataset #091802), (c) 100 RPM (dataset #091803), (d) 125 RPM, (e) 150 RPM.

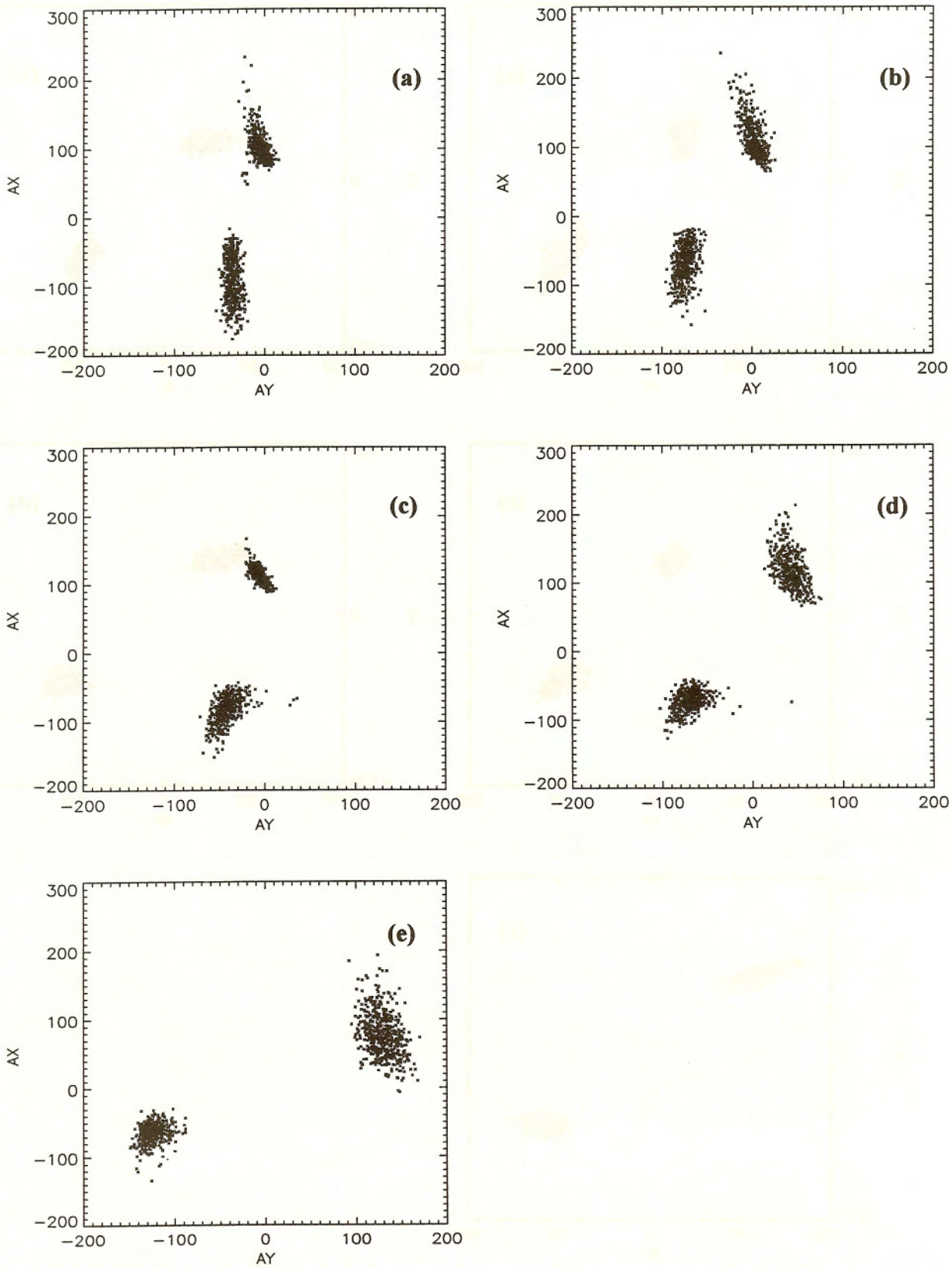

Fig. 4.7. Positive-going Poincaré sections for $A_z = 0$: (a) 75 RPM, (b) 100 RPM (dataset #091802), (c) 100 RPM (dataset #091803), (d) 125 RPM, (e) 150 RPM.

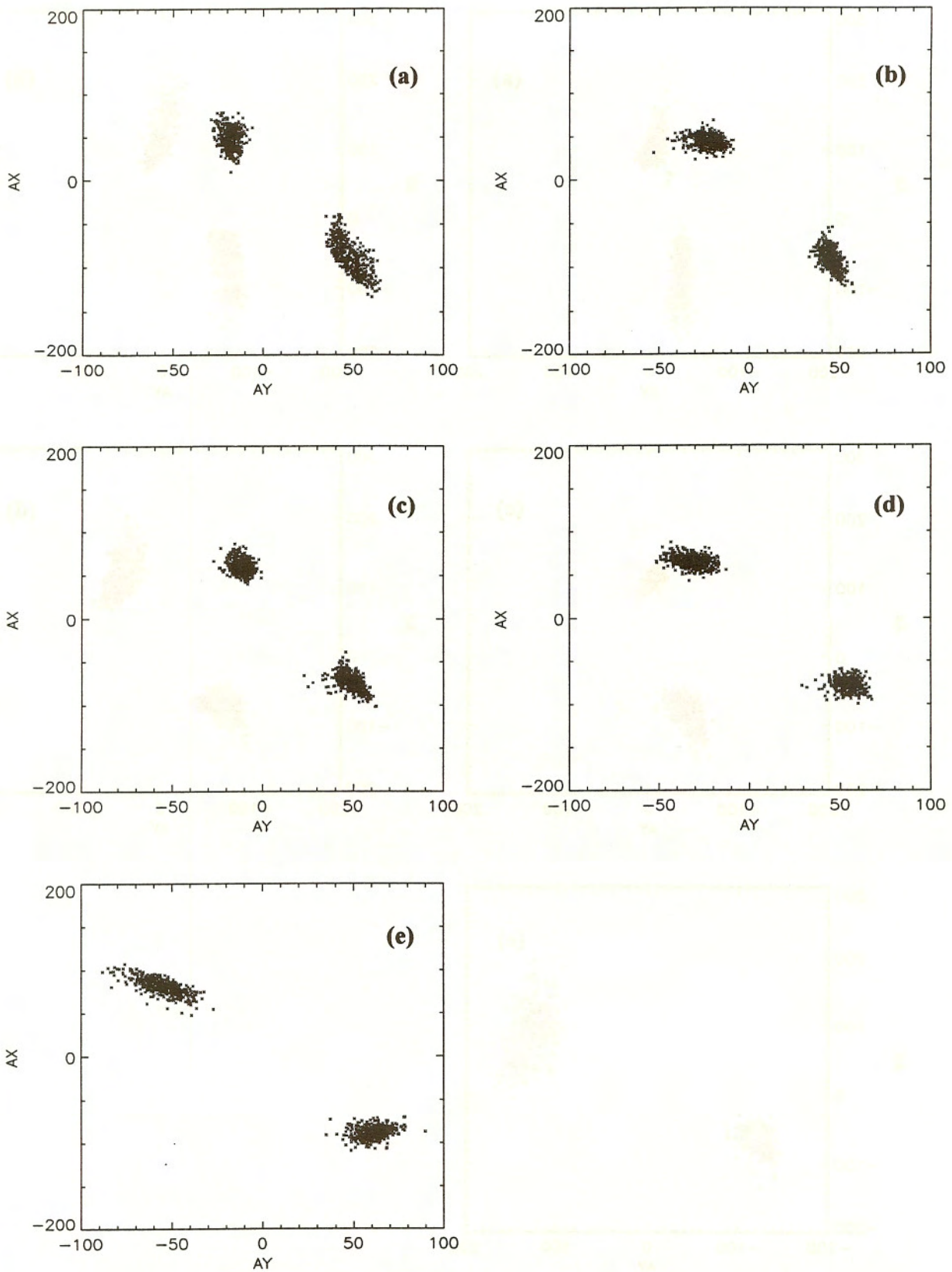

Fig. 4.8. Negative-going Poincaré sections for $A_z = 0$: (a) 75 RPM, (b) 100 RPM (dataset #091802), (c) 100 RPM (dataset #091803), (d) 125 RPM, (e) 150 RPM.

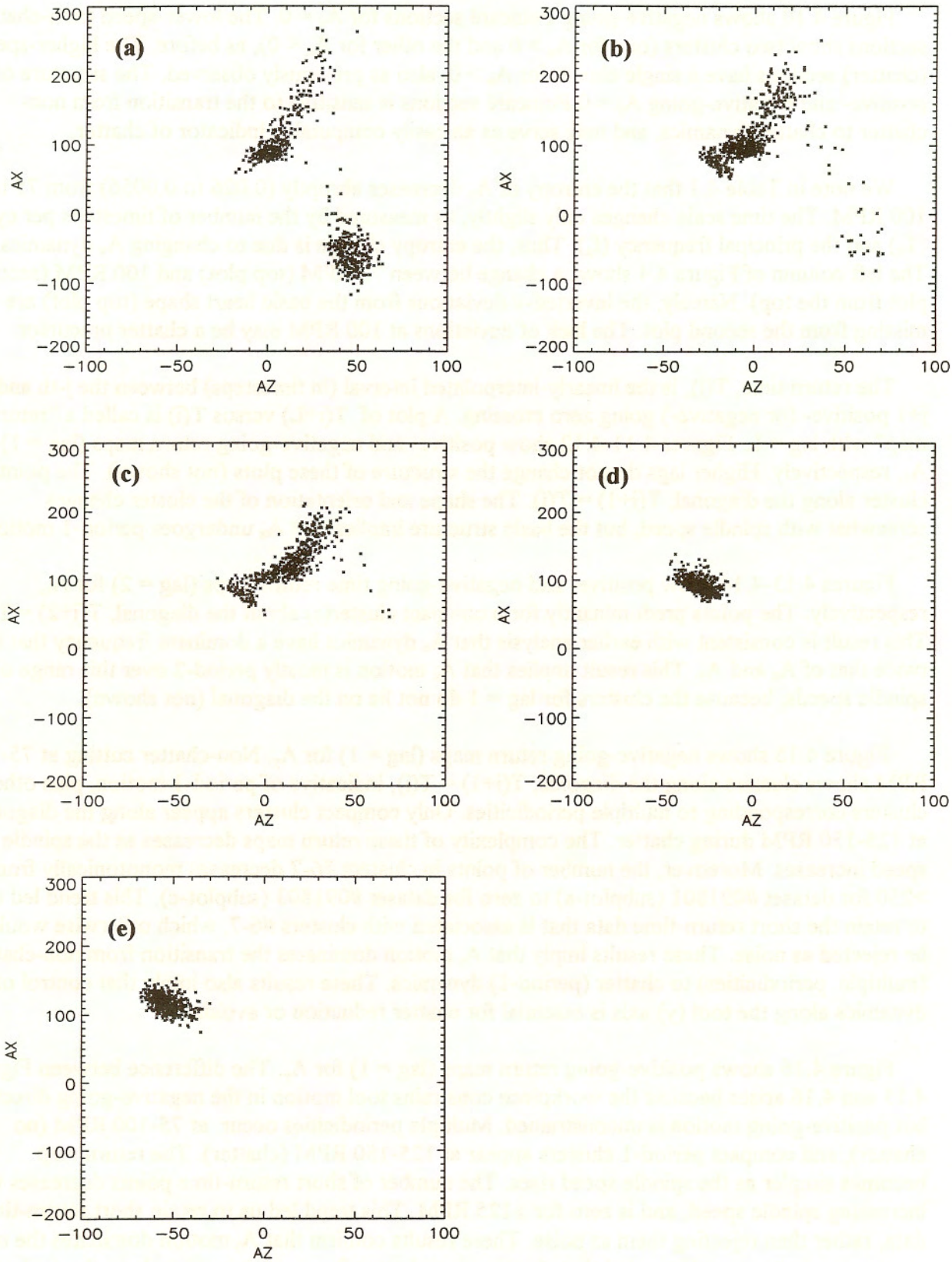

Fig. 4.9. Positive-going Poincaré sections for $A_y = 0$: (a) 75 RPM, (b) 100 RPM (dataset #091802), (c) 100 RPM (dataset #091803), (d) 125 RPM, (e) 150 RPM.

Figure 4.10 shows negative-going Poincaré sections for $A_y = 0$. The lower-speed (non-chatter) sections show two clusters (one for $A_x > 0$ and the other for $A_x < 0$), as before. The higher-speed (chatter) sections have a single cluster for $A_x > 0$, also as previously observed. The structure of positive- and negative-going $A_y = 0$ Poincaré sections is sensitive to the transition from non-chatter to chatter dynamics, and may serve as an easily computable indicator of chatter.

We note in Table 4.1 that the entropy of A_y decreases abruptly (0.026 to 0.0056) from 75 to 100 RPM. The time scale changes only slightly, as measured by the number of timesteps per cycle (T_c) and the principal frequency (f_p). Thus, the entropy change is due to changing A_y dynamics. The left column of Figure 4.4 shows a change between 75 RPM (top plot) and 100 RPM (second plot from the top). Namely, the inverted-v deviations from the basic heart shape (top plot) are missing from the second plot. The lack of deviations at 100 RPM may be a chatter precursor.

The return time, T(j), is the linearly-interpolated interval (in timesteps) between the j-th and j+1 positive- (or negative-) going zero crossing. A plot of T(i+L) versus T(i) is called a "return map" with lag = L. Figures 4.11-4.12 show positive- and negative-going return maps (lag = 1) for A_x, respectively. Higher lags do not change the structure of these plots (not shown). The points cluster along the diagonal, T(i+1) = T(i). The shape and orientation of the cluster changes somewhat with spindle speed, but the basic structure implies that A_x undergoes period-1 motion.

Figures 4.13-4.14 show positive- and negative-going time return maps (lag = 2) for A_z, respectively. The points predominantly form compact cluster(s) about the diagonal, T(i+2) = T(i). This result is consistent with earlier analysis that A_z dynamics have a dominant frequency that is twice that of A_x and A_y. This result implies that A_z motion is mostly period-2 over this range of spindle speeds, because the clusters for lag = 1 do not lie on the diagonal (not shown).

Figure 4.15 shows negative-going return maps (lag = 1) for A_y. Non-chatter cutting at 75-100 RPM shows clusters along the diagonal, T(i+1) = T(i), indicative of period-1 motion, plus other clusters corresponding to multiple periodicities. Only compact clusters appear along the diagonal at 125-150 RPM during chatter. The complexity of these return maps decreases as the spindle speed increases. Moreover, the number of points in clusters #6-7 decreases monotonically from >250 for dataset #091801 (subplot-a) to zero for dataset #091803 (subplot-c). This trend led us to retain the short return-time data that is associated with clusters #6-7, which otherwise would be rejected as noise. These results imply that A_y motion dominates the transition from non-chatter (multiple periodicities) to chatter (period-1) dynamics. These results also imply that control of dynamics along the tool (y) axis is essential for chatter reduction or avoidance.

Figure 4.16 shows positive-going return maps (lag = 1) for A_y. The difference between Figs. 4.15 and 4.16 arises because the workpiece constrains tool motion in the negative-going direction, but positive-going motion is unconstrained. Multiple periodicities occur at 75-100 RPM (no chatter), and compact period-1 clusters appear at 125-150 RPM (chatter). The return map becomes simpler as the spindle speed rises. The number of short return-time points decreases with increasing spindle speed, and is zero for ≥125 RPM. This trend led us to retain short return-time data, rather than rejecting them as noise. These results confirm that A_y motion dominates the non-chatter-to-chatter transition, and that chatter control must focus on dynamics along the tool axis.

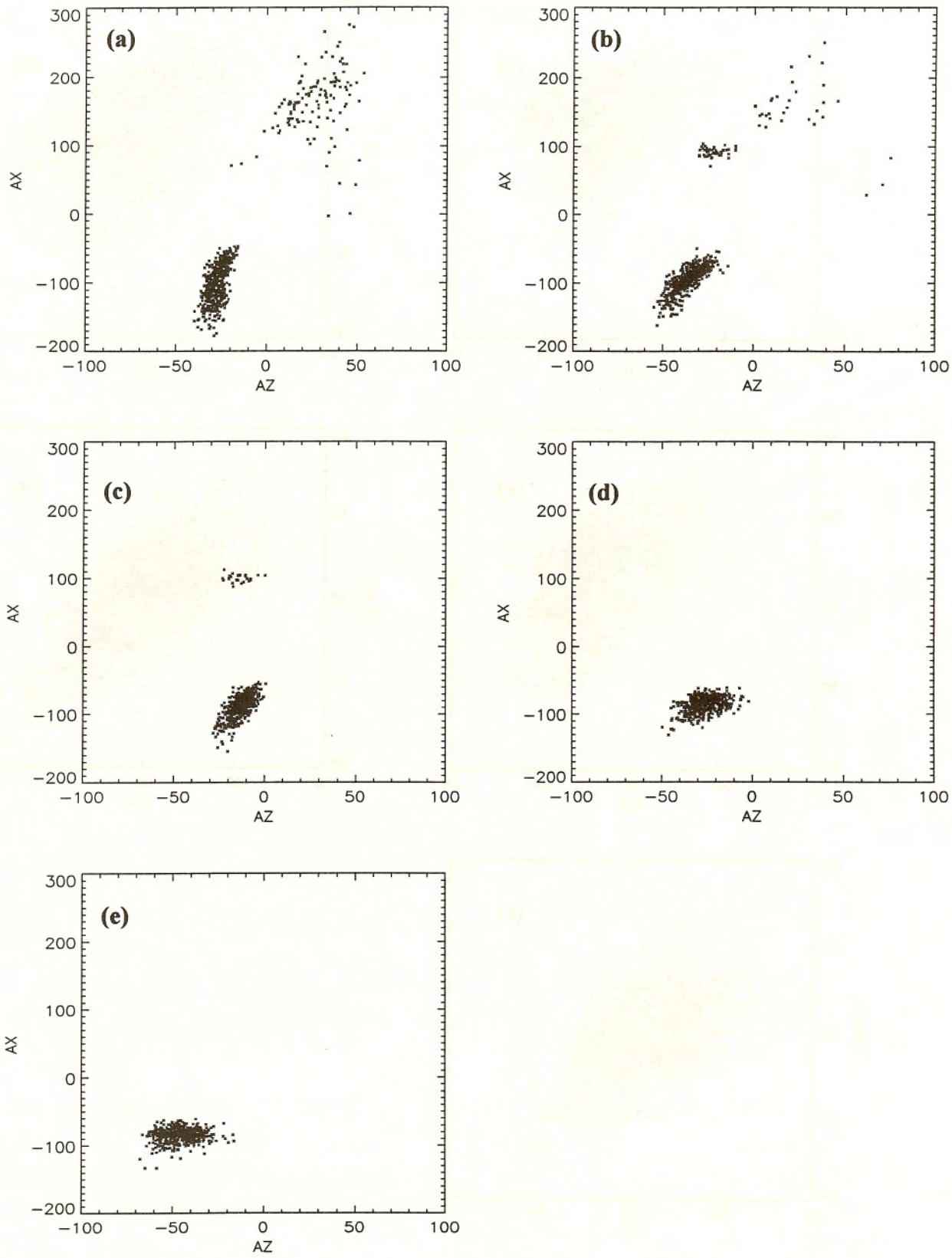

Fig. 4.10. Negative-going Poincaré sections for $A_y = 0$: (a) 75 RPM, (b) 100 RPM (dataset #091802), (c) 100 RPM (dataset #091803), (d) 125 RPM, (e) 150 RPM.

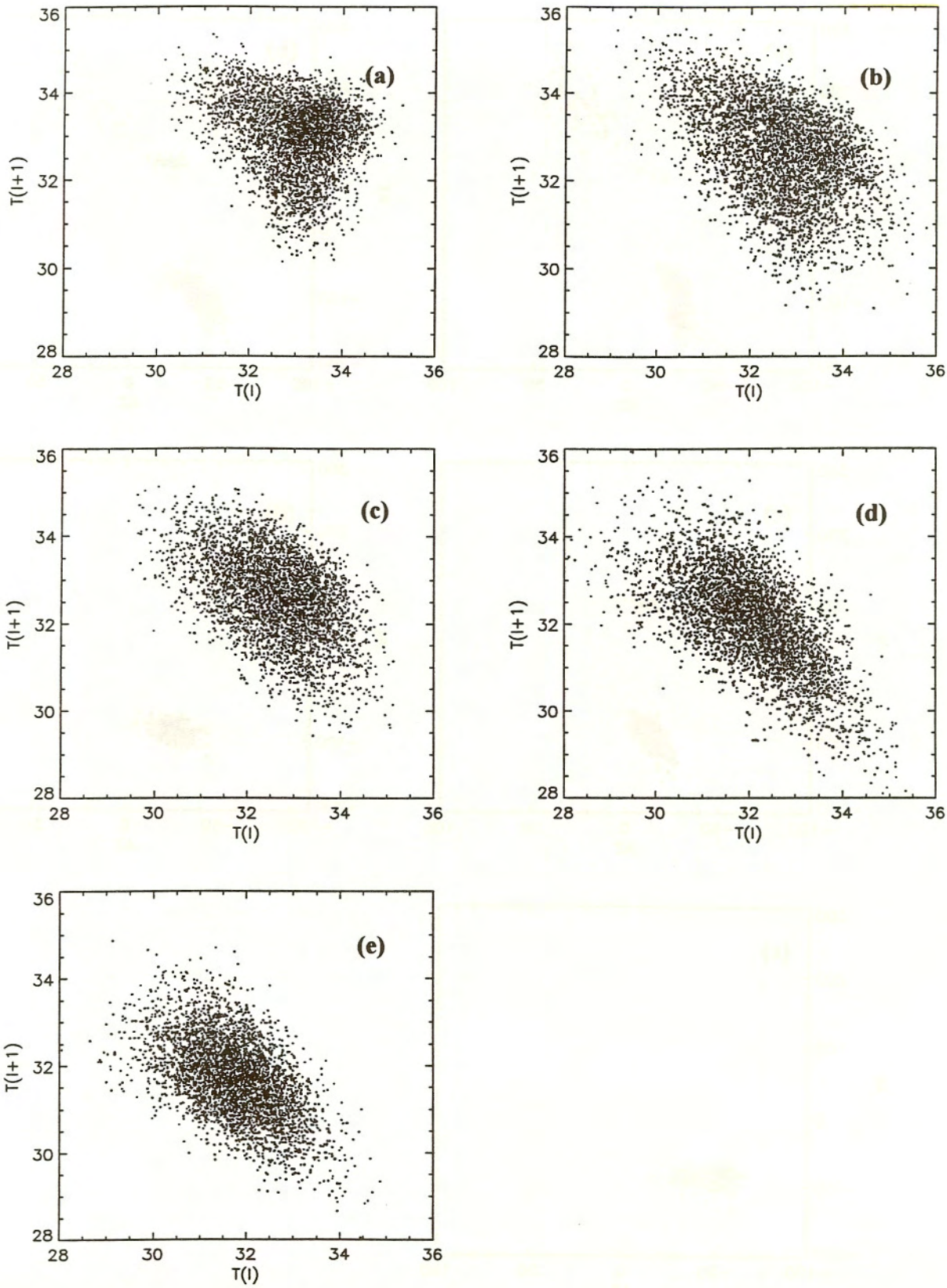

Fig. 4.11. Positive-going return maps (lag = 1) for $A_x = 0$: (a) 75 RPM, (b) 100 RPM (dataset #091802), (c) 100 RPM (dataset #091803), (d) 125 RPM, (e) 150 RPM.

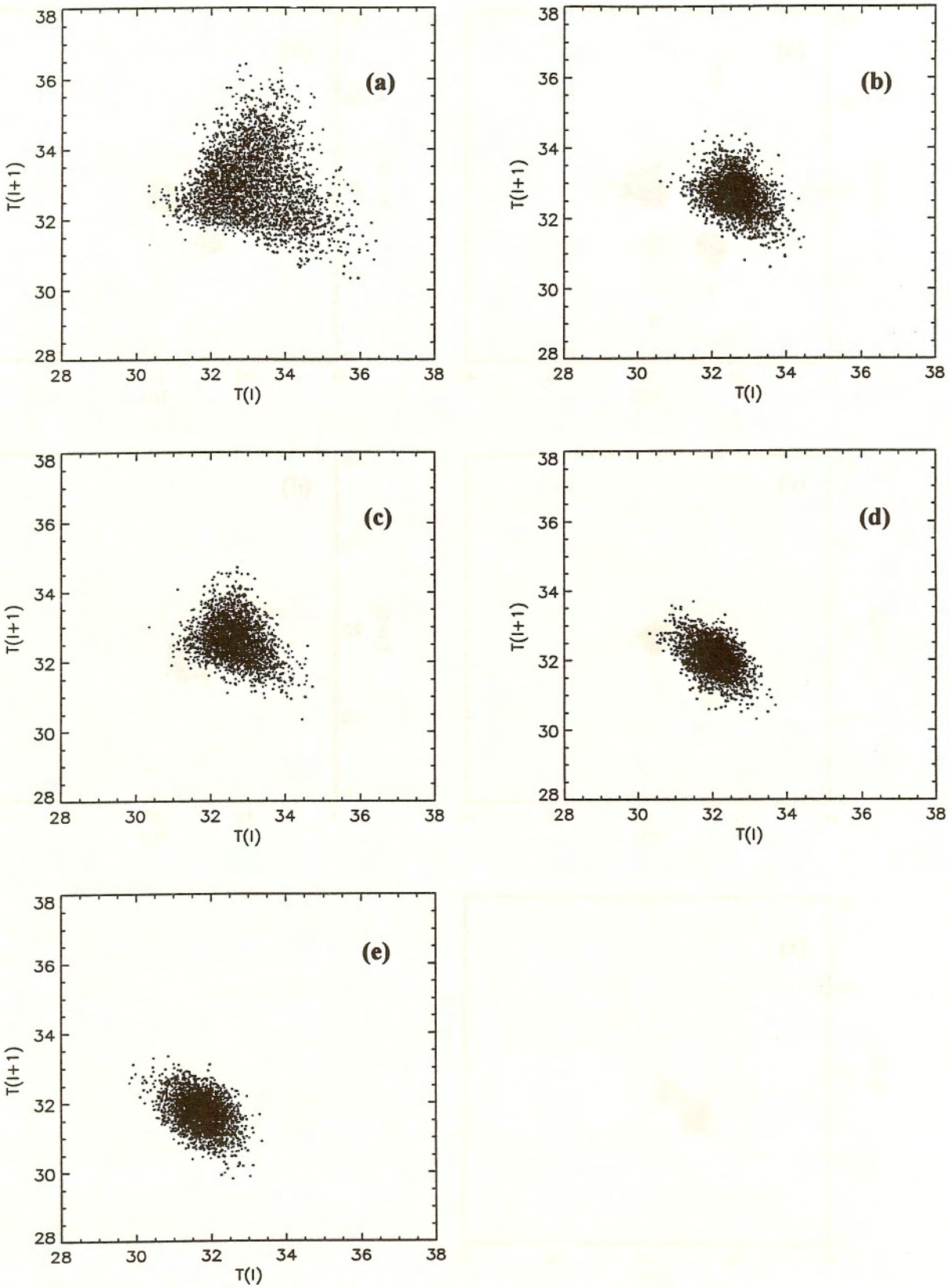

Fig. 4.12. Negative-going return maps (lag = 1) for $A_x = 0$: (a) 75 RPM, (b) 100 RPM (dataset #091802), (c) 100 RPM (dataset #091803), (d) 125 RPM, (e) 150 RPM.

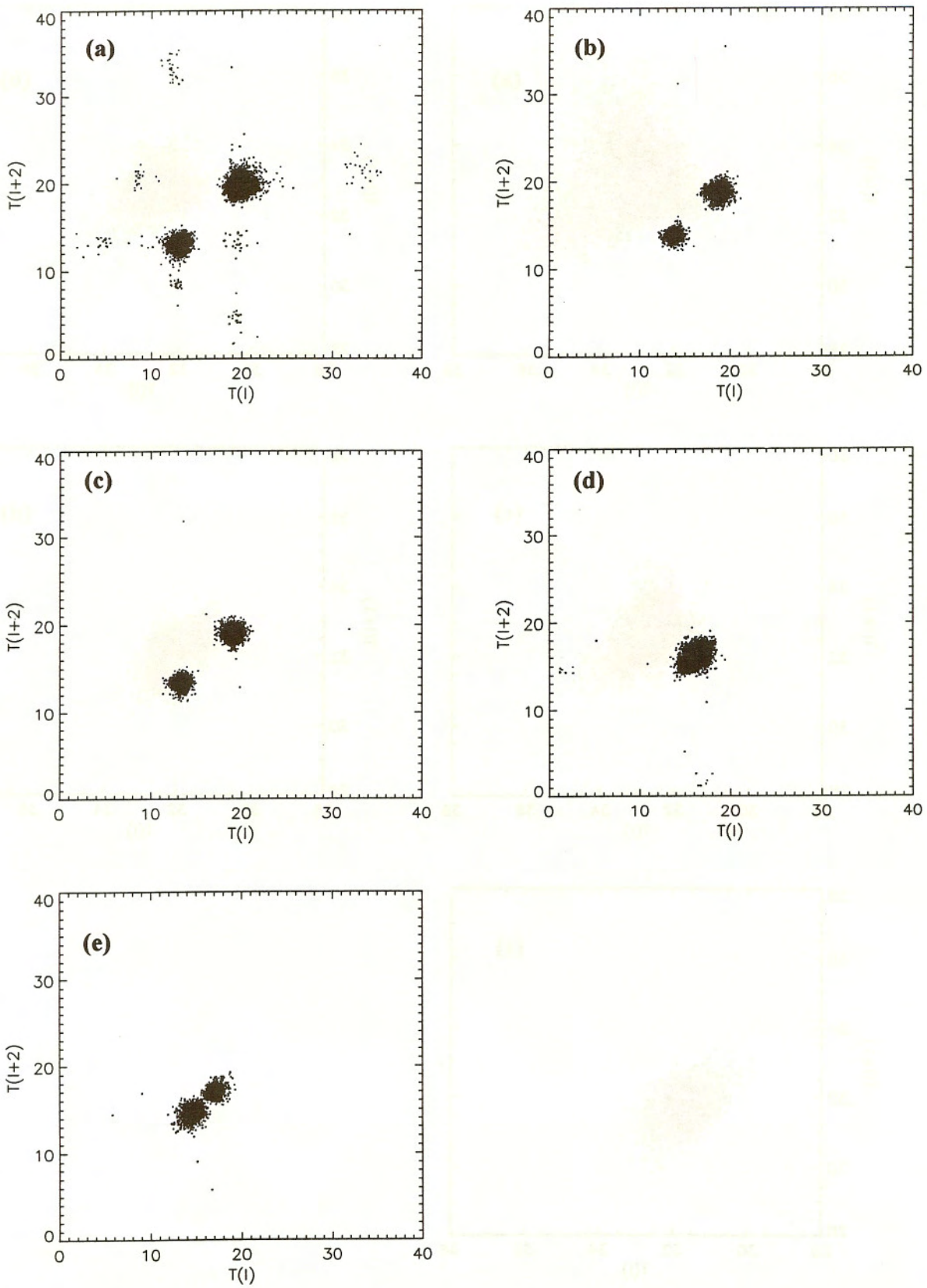

Fig. 4.13. Positive-going return maps (lag = 2) for $A_z = 0$: (a) 75 RPM, (b) 100 RPM (dataset #091802), (c) 100 RPM (dataset #091803), (d) 125 RPM, (e) 150 RPM.

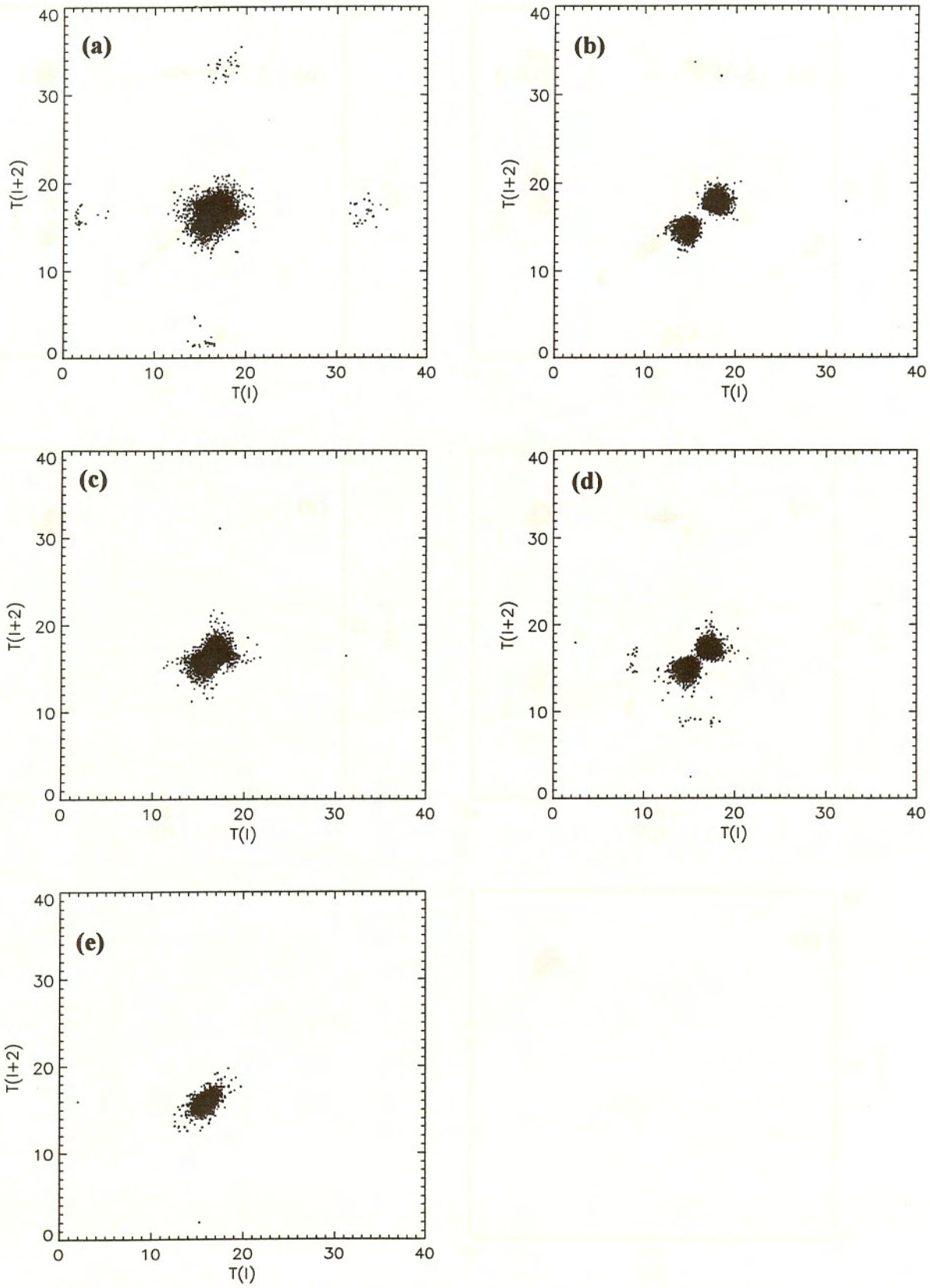

Fig. 4.14. Negative-going return maps (lag = 2) for $A_z = 0$: (a) 75 RPM, (b) 100 RPM (dataset #091802), (c) 100 RPM (dataset #091803), (d) 125 RPM, (e) 150 RPM.

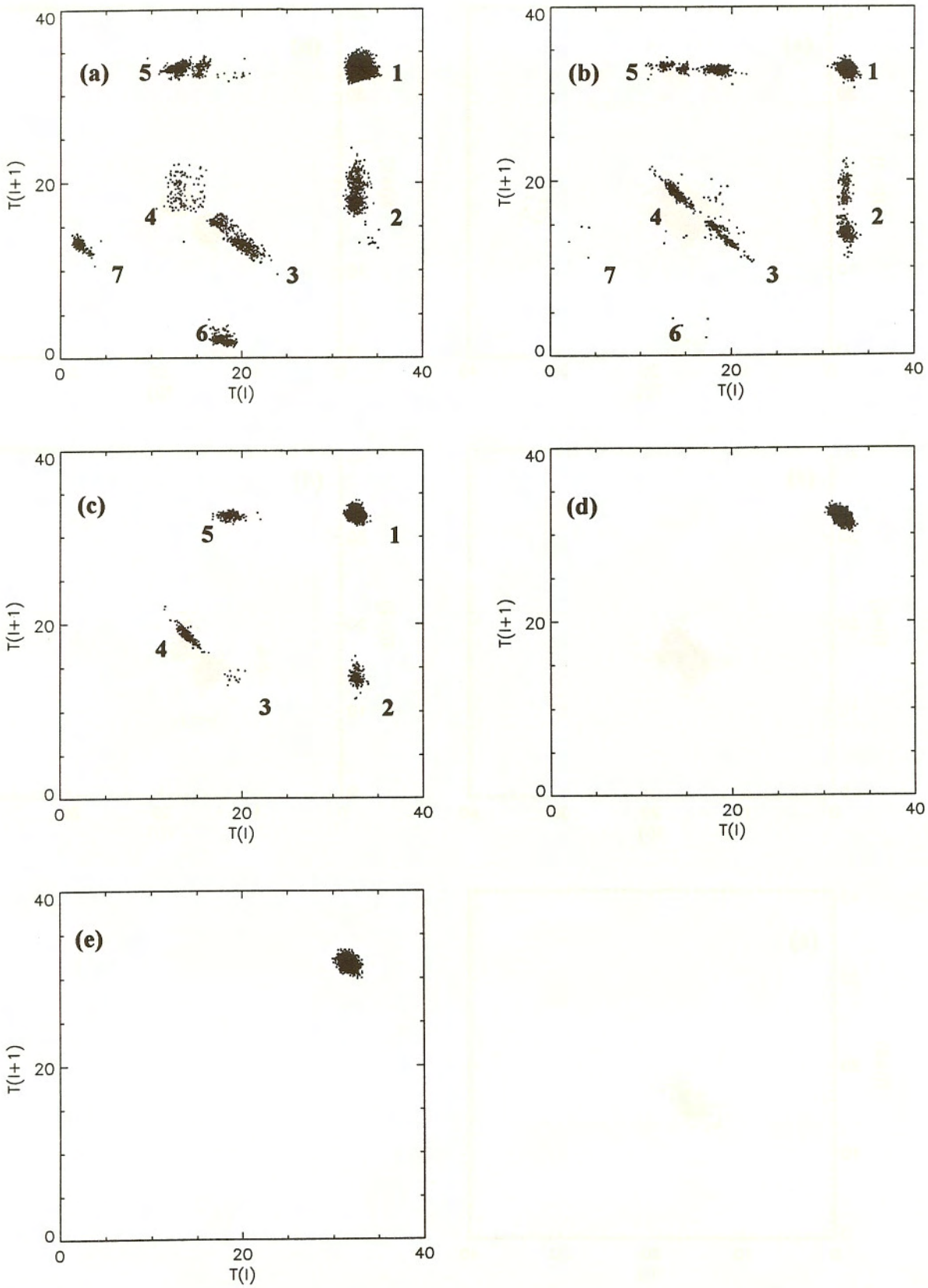

Fig. 4.15. Negative-going return maps (lag = 1) for $A_y = 0$: (a) 75 RPM, (b) 100 RPM (dataset #091802), (c) 100 RPM (dataset #091803), (d) 125 RPM, (e) 150 RPM.

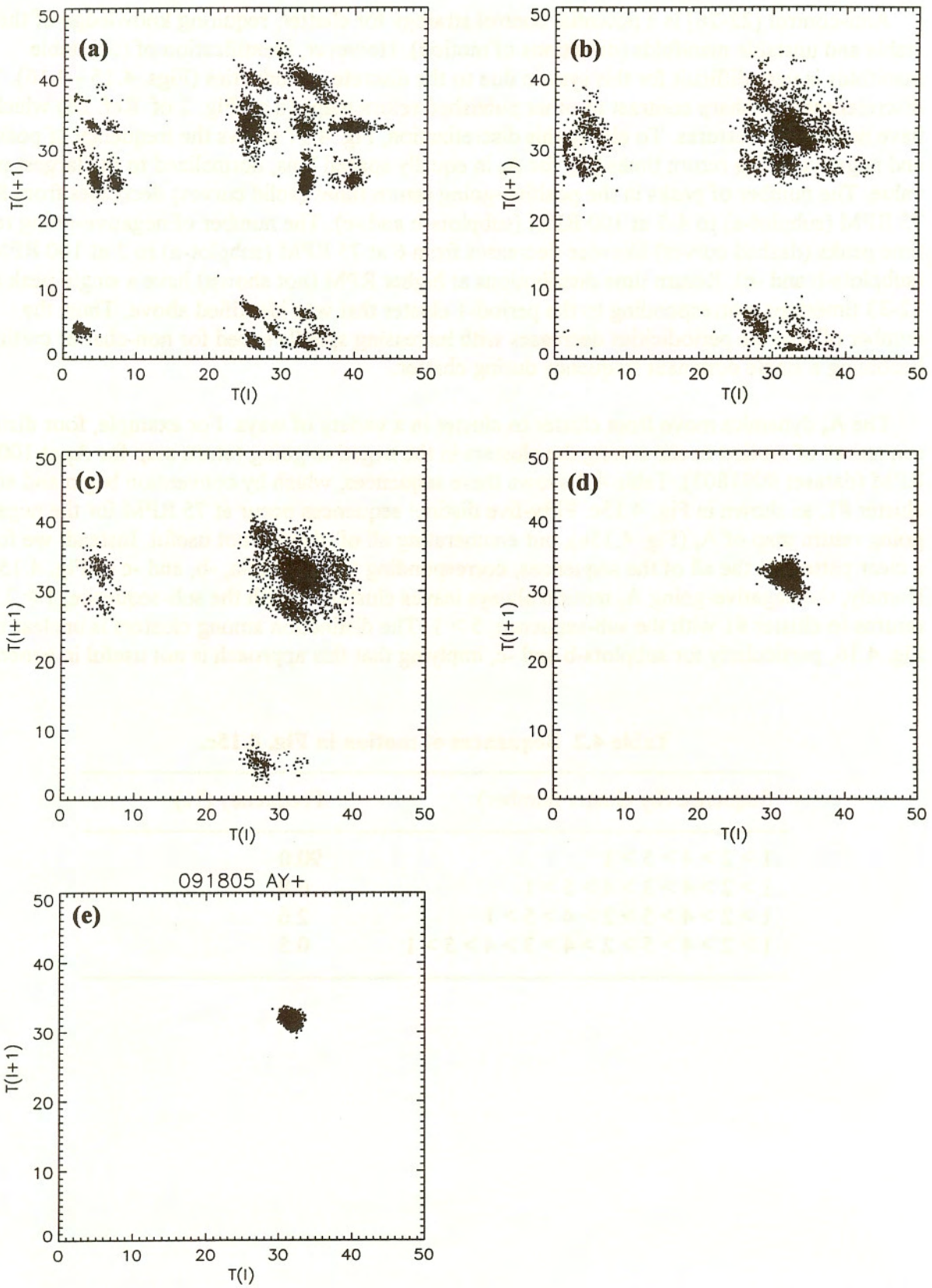

Fig. 4.16. Positive-going return maps (lag = 1) for $A_y = 0$: (a) 75 RPM, (b) 100 RPM (dataset #091802), (c) 100 RPM (dataset #091803), (d) 125 RPM, (e) 150 RPM.

Anti-control [22-26] is a potential control strategy for chatter, requiring knowledge of the stable and unstable manifolds (directions of motion). However, identification of (un)stable manifolds is very difficult for this system due to the discrete periodicities (Figs. 4.15 - 4.16). This discreteness is in sharp contrast to other published return maps (e.g., Fig. 2 of Ref. 26) which have no discrete features. To clarify this discretization, Fig. 4.17 shows the frequency of positive- and negative-going return times (T_i) for A_y in equally spaced bins, normalized to the largest peak value. The number of peaks in the positive-going return times (solid curves) decreases from 8 at 75 RPM (subplot-a) to 4-5 at 100 RPM (subplots-b and -c). The number of negative-going return time peaks (dashed curves) likewise decreases from 6 at 75 RPM (subplot-a) to 3 at 100 RPM (subplots-b and -c). Return time distributions at higher RPM (not shown) have a single peak at 32-33 timesteps, corresponding to the period-1 cluster that was identified above. Thus, the number of discrete periodicities decreases with increasing spindle speed for non-chatter cutting, becoming a single dominant frequency during chatter.

The A_y dynamics move from cluster to cluster in a variety of ways. For example, four distinct sequences of motion occur among the clusters in the negative-going return map for A_y at 100 RPM (dataset #091803). Table 4.2 shows these sequences, which by convention begin and end at cluster #1, as shown in Fig. 4.15c. Fifty-five distinct sequences occur at 75 RPM for the negative-going return map of A_y (Fig. 4.15a), but enumerating all of them is not useful. Instead, we found a clear pattern in the all of the sequences, corresponding to subplots-a, -b, and -c of Fig. 4.15. Namely, the negative-going A_y motion always leaves cluster #1 with the sub-sequence, 1 > 2, and returns to cluster #1 with the sub-sequence, 5 > 1. The distinction among clusters is unclear in Fig. 4.16, particularly for subplots-b and -c, implying that this approach is not useful in general.

Table 4.2 Sequences of motion in Fig. 4.15c.

Sequence (by cluster number)	Frequency (%)
1 > 2 > 4 > 5 > 1	90.0
1 > 2 > 4 > 3 > 4 > 5 > 1	6.8
1 > 2 > 4 > 5 > 2 > 4 > 5 > 1	2.6
1 > 2 > 4 > 5 > 2 > 4 > 3 > 4 > 5 > 1	0.5

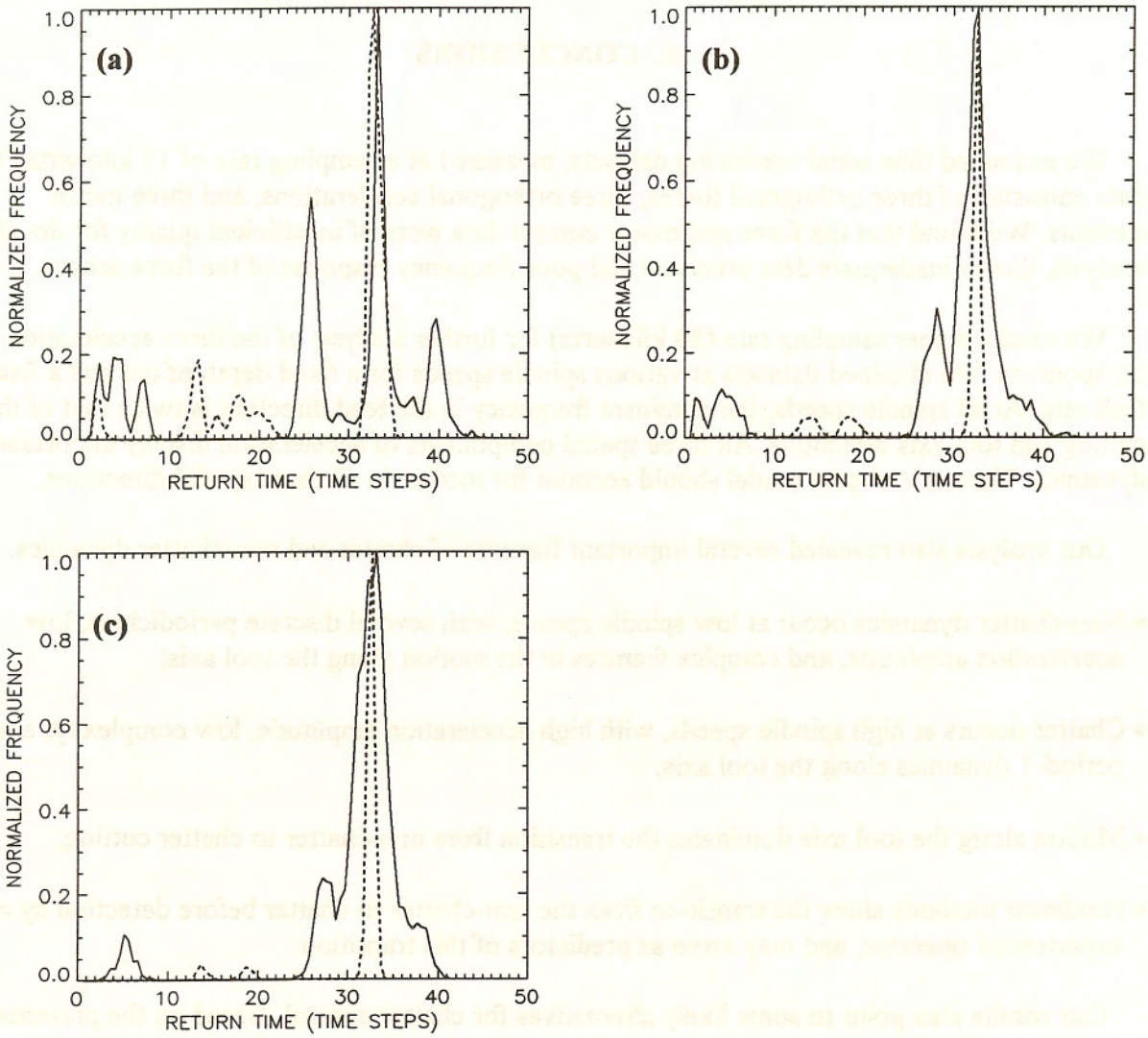

Fig. 4.17. Normalized frequency distribution of postive-going (solid curves) and negative-going (dashed curves) return times for $A_y = 0$ from: (a) dataset #091801 (75 RPM), (b) dataset #091802 (100 RPM), and (c) dataset #091803 (100 RPM).

5. CONCLUSIONS

We examined time serial machining datasets, measured at a sampling rate of 15 kilohertz. The data consisted of three orthogonal forces, three orthogonal accelerations, and three motor currents. We found that the force and motor current data were of insufficient quality for detailed analysis, due to inadequate data precision and poor frequency response of the force sensor.

We used a higher sampling rate (50 kilohertz) for further analysis of the three acceleration components. We obtained datasets at various spindle speeds for a fixed depth of cut and a fixed feed rate. At all spindle speeds, the dominant frequency in the feed direction is twice that of the cutting and tool axis directions. All three spatial components of acceleration display important dynamics. Thus, a tool-part model should account for motion in all three spatial directions.

Our analysis also revealed several important features of chatter and non-chatter dynamics.

- Non-chatter dynamics occur at low spindle speeds, with several discrete periodicities, low acceleration amplitude, and complex features in the motion along the tool axis;

- Chatter occurs at high spindle speeds, with high acceleration amplitude, low complexity, and period-1 dynamics along the tool axis;

- Motion along the tool axis dominates the transition from non-chatter to chatter cutting;

- Nonlinear methods show the transition from the non-chatter to chatter before detection by an experienced operator, and may serve as predictors of this transition.

Our results also point to some likely alternatives for chatter control. Based on the presence of multiple periodicities during non-chatter cutting, we hypothesize that enhancement of low-amplitude chaos along the tool axis may suppress chatter. For example, chatter may be inhibited by chaos "anti-control," i.e., feedback control that enhances or maintains chaos. Another potential control strategy involves feedback changes that have the effect of mechanically damping the period-1 motion (dynamic damping) along the tool axis. We hope to pursue such approaches in subsequent work.

ACKNOWLEDGMENTS

We thank W. E. Barkman, R. F. Holdaway, V. A. Protopopescu, and J. F. Thomas, for their valuable comments on our work. We also gratefully acknowledge the encouragement and programmatic support of this work by W. E. Barkman and C. S. Robinson.. This research was sponsored by the U.S. Department of Energy, Office of Defense Programs, under CRADA #Y1295-0357. The work was performed at Oak Ridge National Laboratory, managed for the United States Department of Energy by Lockheed Martin Energy Research Corporation, under Contract No. DE-AC05-96OR22464.

REFERENCES

1. B. S. Berger, M. Rokni, and I. Minis, "The nonlinear dynamics of metal cutting," *Int. J. Engng. Sci.* **30,** 1433-1440 (1992).

2. I. Grabec, "Chaos generated by the cutting process," *Phys. Lett. A* **117,** 384-386 (1986).

3. I. Grabec, "Chaotic vibrations and acoustic emission caused by the cutting process," *Proc 8th Int. Acoustic Emissions Symp.* (Tokyo, Japan) 1986, pp. 87-93.

4. I. Grabec, "Chaotic dynamics of the cutting process," *Int. J. Mach. Tools Manufact.* **28,** 19-32 (1988).

5. K. Jemielniak and A. Widota, "The development of frequency and amplitude of chatter vibration," *Int. J. Mach. Tools Manufact.* **29**, 249-256 (1989).

6. J. S. Lin and C. I. Weng, "A nonlinear dynamic model of cutting," *Int. J. Mach. Tools Manufact.* **30**, 53-64 (1990).

7. L. Qu, A. Xie, and X. Li, "Study and performance evaluation of some nonlinear diagnostic methods for large rotating machines," *Mech. Mach. Theory* **28**, 699-713 (1993).

8. D. W. Wu and C. R. Liu, "An analytical Model of cutting dynamics. Part 1: model building," *J. Engng. for Industry* **107,** 107-111 (1985).

9. D. W. Wu and C. R. Liu, "An analytical Model of cutting dynamics. Part 2: verification," *J. Engng. for Industry* **107**, 112-118 (1985).

10. S. T. S. Bukkapatnam, A. Lakhtakia, and S. R. T. Kumara, "Analysis of sensor signals shows turning on a lathe exhibits low-dimensional chaos," *Phys. Rev. E* **52**, 2375-2387 (1995).

11. L. M. Hively, N. E. Clapp, C. S. Daw, W. F. Lawkins, and M. L. Eisenstadt "Nonlinear Analysis of EEG for Epileptic Seizures," *ORNL/TM-12961*, Oak Ridge National Laboratory, Oak Ridge, TN. (1995).

12. J. C. Schouten, F. Takens, and C. M. van den Bleek, "Estimation of the Dimension of a Noisy Attractor," *Phys. Rev. E* **50**, 1851-1861 (1994).

13. C. E. Shannon and W. Weaver, *The Mathematical Theory of Communication*, University of Illinois Press, Urbana, 1949.

14. A. M. Fraser and H. L. Swinney, "Independent Coordinates for Strange Attractors from Mutual Information," *Phys. Rev A* **33**, 1134-1140 (1986).

15. F. Takens, "On the Numerical Determination of the Dimension of an Attractor," in *Dynamical Systems and Bifurcations*, ed. B.L.J. Braaksma, H.W. Broer, and F. Takens, *Lecture Notes in Mathematics* **1125**, Springer-Verlag, Berlin (1984) pp. 99-106.

16. J. C. Schouten, F. Takens, and C. M. van den Bleek, "Maximum-Likelihood Estimation of the Entropy of an Attractor," *Phys. Rev. E* **49**, 126-129 (1994).

17. H. D. I. Abarbanel, R. Brown, J.J. Sidorowich, and L. Sh. Tsimring, "The Analysis of Observed Chaotic Data in Physical Systems," *Rev. Mod. Phys.* **65**, 1331-1392 (1993).

18. P. Grassberger, T. Schreiber, C. Schaffrath, "Nonlinear Time Sequence Analysis," *Int. J. Bifur. Chaos* **3**, 521-547 (1991).

19. N. H. Packard, J. P. Crutchfield, J. D. Farmer, and R. S. Shaw, *Phys. Rev. Lett.* **45**, 712 (1980)

20. F. Takens, "Detecting Strange Attractors in Turbulence," in *Lecture Notes in Mathematics*, ed. by D.A. Rand and L.-S. Young, Springer, Berlin, 1981, pp. 366.

21. D. S. Broomhead and G.P. King, "Extracting Qualitative Dynamics from Experimental Data," *Physica D* **20**, 217-236 (1986).

22. Y-C. Lai, C. Grebogi, "Converting Transient Chaos into Sustained Chaos by Feedback Control," *Phys. Rev. E* 49 (1994) 1094-1098.

23. W. Yang, M. Ding, A. J. Mandell, E. Ott, "Preserving Chaos: Control Strategies to Preserve Complex Dynamics with Potential Relevance to Biological Disorders," *Phys. Rev. E* 51 (1995) 102-110.

24. Y. Nagai, Y.-C. Lai, "Selection of a Desirable Chaotic Phase Using Small Feedback Control," *Phys. Rev. E* 51 (1995) 3842-3848.

25. V. In, S. E. Mahan, W.L. Ditto, M.L. Spano, "Experimental Maintenance of Chaos," *Phys. Rev. Lett.* 74 (1995) 4420-4423.

26. S. J. Schiff, K. Jerger, D. H. Duong, T. Chang, M. L. Spano, W. L. Ditto, "Controlling Chaos in the Brain," *Nature* 370 (1994) 615-620.

DISTRIBUTION

M. A. Akerman
W. E. Barkman
B. A. Berven
N. E. Clapp
V. H. Dale
W. K. Dagenhart
C. S. Daw
D. J. Downing
P.C. Gailey
R. G. Gilliland
L. M. Hively
R. F. Holdaway
M. R. Kennel
W. F. Lawkins
R. W. Leggett
M. R. Leuze
G. T. Mays
G. W. Morrison
C. E. Oliver
V. A. Protopopescu
D. E. Reichle
S. C. Robinson
R. M. Schilling, Jr.
R. M. Sincovec
S. F. Smith
T. P. Sjoreen
J. O. Stiegler
J. F. Thomas
B. E. Tonn
D. W. Walker
D. E. Welch
Laboratory Records - RC
Laboratory Records (2 copies)
Patent Office